

# 1           **Is the recovery of stratospheric O<sub>3</sub> speeding up in the Southern Hemisphere?**

## 2                           **An evaluation from the first IASI decadal record (2008-2017)**

3  
4 Catherine Wespes<sup>1</sup>, Daniel Hurtmans<sup>1</sup>, Simon Chabrillat<sup>2</sup>, Gaétane Ronsmans<sup>1</sup>, Cathy  
5 Clerbaux<sup>3,1</sup> and Pierre-François Coheur<sup>1</sup>

6 <sup>1</sup>Université Libre de Bruxelles (ULB), Faculté des Sciences, Chimie Quantique et  
7 Photophysique, Bruxelles, Belgique

8 <sup>2</sup>Belgian Institute for Space Aeronomy, Brussels, Belgium

9 <sup>3</sup>LATMOS/IPSL, Sorbonne Université, UVSQ, CNRS, Paris, France

### 10 11 **Abstract**

12 In this paper, we present the global fingerprint of recent changes in the mid-upper stratospheric  
13 (MUS<sub>t</sub>; <25hPa) ozone (O<sub>3</sub>) in comparison with the lower stratospheric (LSt; 150-25 hPa) O<sub>3</sub>  
14 derived from the first 10 years of the IASI/Metop-A satellite measurements (January 2008 –  
15 December 2017). The IASI instrument provides vertically-resolved O<sub>3</sub> profiles with very high  
16 spatial and temporal (twice daily) samplings, allowing to monitor O<sub>3</sub> changes in these two  
17 regions of the stratosphere. By applying multivariate regression models with adapted geophysical  
18 proxies on daily mean O<sub>3</sub> time series, we discriminate anthropogenic trends from various modes  
19 of natural variability, such as the El Niño/Southern Oscillation – ENSO. The representativeness  
20 of the O<sub>3</sub> response to its natural drivers is first examined. One important finding relies on a  
21 pronounced contrast between a positive LSt O<sub>3</sub> response to ENSO in the extra-tropics and a  
22 negative one in the tropics, with a delay of 3 months, which supports a stratospheric pathway for  
23 the ENSO influence on lower stratospheric and tropospheric O<sub>3</sub>. In terms of trends, we find an  
24 unequivocal O<sub>3</sub> recovery from the available period of measurements in winter/spring at mid-high  
25 latitudes for the two stratospheric layers sounded by IASI (>~35°N/S in the MUS<sub>t</sub> and >~45°S in  
26 the LSt) as well as in the total columns at southern latitudes (>~45°S) where the increase reaches  
27 its maximum. These results confirm the effectiveness of the Montreal protocol and its  
28 amendments, and represent the first detection of a significant recovery of O<sub>3</sub> concurrently in the  
29 lower, in the mid-upper stratosphere and in the total column from one single satellite dataset. A  
30 significant decline in O<sub>3</sub> at northern mid-latitudes in the LSt is also detected, especially in  
31 winter/spring of the northern hemisphere. Given counteracting trends in LSt and MUS<sub>t</sub> at these  
32 latitudes, the decline is not categorical in total O<sub>3</sub>. When freezing the regression coefficients  
33 determined for each natural driver over the whole IASI period but adjusting a trend, we calculate  
34 a significant speeding up in the O<sub>3</sub> response to the decline of O<sub>3</sub> depleting substances (ODS) in  
35 the total column, in the LSt and, to a lesser extent, in the MUS<sub>t</sub>, at high southern latitudes over  
36 the year. Results also show a small significant acceleration of the O<sub>3</sub> decline at northern mid-  
37 latitudes in the LSt and in the total column over the last years. That, specifically, needs urgent  
38 investigation for identifying its exact origin and apprehending its impact on climate change.

39 Additional years of IASI measurements would, however, be required to confirm the O<sub>3</sub> change  
40 rates observed in the stratospheric layers over the last years.

41

## 42 **1 Introduction**

43

44 Ozone is a key radiatively active gas of the Earth atmosphere, in both the troposphere and the  
45 stratosphere. While, in the troposphere, O<sub>3</sub> acts as a strong pollutant and an important  
46 greenhouse gas, in the stratosphere and, more particularly, in the middle-low stratosphere, it  
47 forms a protective layer for life on Earth against harmful solar radiation. In the 1980s, the  
48 scientific community motivated decision-makers to regulate the use of chlorofluorocarbons  
49 (CFCs), after the unexpected discovery of the springtime Antarctic ozone hole (Chubachi, 1984;  
50 Farman et al., 1985) that was suspected to be induced by continued use of CFCs (Molina and  
51 Rowland, 1974; Crutzen, 1974). The O<sub>3</sub> depletion was later verified from measurements at other  
52 Antarctic sites (e.g. Farmer et al., 1987) and from satellite observations (Stolarski et al., 1986),  
53 and explained by the role of CFC's on the massive destruction of O<sub>3</sub> following heterogeneous  
54 reactions on the surface of polar stratospheric clouds (Solomon, 1986; 1999 and references  
55 therein). The world's nations reacted to that human-caused worldwide problem by ratifying the  
56 International Vienna Convention for the Protection of the Ozone Layer in 1985 and the Montreal  
57 Protocol in 1987 with its later amendments, which forced the progressive banning of these ozone  
58 depleting substances (ODS) in industrial applications by early 1990s with a total phase-out of the  
59 most harmful CFCs by the year 2000.

60

61 A recovery from O<sub>3</sub> depletion is expected in response to the Montreal Protocol and its  
62 amendments, but with a delayed period due to the long residence time of halocarbons in the  
63 atmosphere (Hofmann et al., 1997; Dhomse el al., 2006; WMO, 2007; 2011). The decline of  
64 CFCs in the stratosphere was only initiated about 10 years after their phasing out (Anderson et  
65 al., 2000; Newman et al., 2006; Solomon et al., 2006 ; Mäder et al., 2010; WMO, 2011; 2014).  
66 The early signs of ozone response to that decline were identified in several studies that reported  
67 first a slowdown in stratospheric ozone depletion (e.g. Newchurch et al., 2003; Yang et al.,  
68 2008), followed by a leveling off of upper stratospheric (e.g. WMO, 2007) and total O<sub>3</sub> (e.g.  
69 WMO, 2011; Shepherd et al., 2014) depletion since the 2000's. A significant onset of recovery  
70 was identified later for upper stratospheric O<sub>3</sub> (e.g. WMO, 2014; 2018; Harris et al., 2015). Only  
71 a few studies have shown evidence for increasing total column O<sub>3</sub> in polar regions during  
72 springtime (e.g. Salby et al., 2011; Kuttippurath et al., 2013; Shepherd et al., 2014; Solomon et  
73 al., 2016). Statistically significant long-term recovery in total O<sub>3</sub> column (TOC) on a global scale  
74 has not yet been observed, likely because of counteracting trends in the different vertical  
75 atmospheric layers. Ball et al. (2018) have found that a continuing O<sub>3</sub> decline prevails in the  
76 lower stratosphere since 1998, leading to a slower increase in total O<sub>3</sub> than expected from the  
77 effective equivalent stratospheric chlorine (EESC) decrease. However, the reported decline is not  
78 reproduced by the state-of-the-art models and its exact reasons are still unknown (Ball et al.,

79 2018). Wargan et al. (2018) and Galytska et al. (2019) recently reported that the decline in the  
80 extratropical lower stratosphere and tropical mid-stratosphere is dynamically controlled by  
81 variations in the tropical upwelling.

82  
83 Although recent papers based on observational datasets and statistical approaches agree that we  
84 currently progress towards an emergence into ozone recovery (e.g. Pawson et al., 2014; Harris et  
85 al., 2015; Steinbrecht et al., 2017; Sofieva et al., 2017; Ball et al., 2018; Weber et al., 2018),  
86 trend magnitude and trend significance over the whole stratosphere substantially differ from one  
87 study to another and, consequently, they are still subject to uncertainty (Keeble et al., 2018). A  
88 clear identification of the onset of O<sub>3</sub> recovery is very difficult due to concurrent sources of O<sub>3</sub>  
89 fluctuations (e.g. Reinsel et al., 2005; WMO, 2007, 2011). They include: changes in solar  
90 ultraviolet irradiance, in atmospheric circulation patterns such as the quasi-biennial oscillation  
91 (QBO; Baldwin et al., 2001) and the El Niño–Southern Oscillation (ENSO; e.g. Randel et al.,  
92 2009), in temperature, in ODS emissions and volcanic eruptions (e.g. Mt Pinatubo in 1991 and  
93 Calbuco in 2015) with their feedbacks on stratospheric temperature and dynamics (e.g. Jonsson  
94 et al., 2004). Furthermore, the differences in vertical/spatial resolution and in retrieval  
95 methodologies (inducing biases), possible instrumental degradations (inducing drifts), and use of  
96 merged datasets into composites, likely explain part of the trend divergence between various  
97 studies. If merging performed on deseasonalized anomalies offers the advantage of removing  
98 instrumental biases between the individual data records (Sofieva et al., 2017), there remains large  
99 differences in anomaly values between the independent datasets, as well as large instrumental  
100 drifts and drift uncertainty estimates that prevent deriving statistically accurate trends (Harris et  
101 al., 2015; Hubert et al., 2016). In this context, there is a pressing need for long-duration, high-  
102 density and homogenized O<sub>3</sub> profile dataset to assess significant O<sub>3</sub> changes in different parts of  
103 the stratosphere and their contributions to the total O<sub>3</sub>.

104  
105 In this paper, we exploit the high frequency (daily) and spatial coverage of the IASI satellite  
106 dataset over the first decade of the mission (January 2008 – December 2017) to determine global  
107 patterns of reliable trends in the stratospheric O<sub>3</sub> records, separately in the Mid-Upper  
108 Stratosphere (MUS<sub>t</sub>) and the Lower Stratosphere (LS<sub>t</sub>). This study is built on previous analysis  
109 of stratospheric O<sub>3</sub> trends from IASI, estimated on latitudinal averages over a shorter period  
110 (2008-2013) (Wespes et al., 2016). A multivariate linear regression (MLR) model (annual and  
111 seasonal formulations) that is similar to that previously used for tropospheric O<sub>3</sub> studies from  
112 IASI (Wespes et al., 2017; 2018), but adapted here for the stratosphere with appropriate drivers,  
113 is applied to gridded daily mean O<sub>3</sub> time series in the MUS<sub>t</sub> and the LS<sub>t</sub>. The MLR model is  
114 evaluated in terms of its performance and its ability to capture the observed variability in Section  
115 2, in terms of representativeness of O<sub>3</sub> drivers in Section 3 and in terms of adjusted trends in  
116 Section 4. The minimum numbers of years of IASI measurements that is required to indeed  
117 detect the adjusted trends from MLR in the two layers is also estimated in Section 4 that ends

118 with an evaluation of the trends detectable in polar winter and spring and with an evaluation of a  
119 speeding up in the O<sub>3</sub> changes.

120

## 121 **2 Dataset and methodology**

122

### 123 **2.1 IASI O<sub>3</sub> data**

124

125 The Infrared Atmospheric Sounding Interferometer (IASI) is a nadir-viewing Fourier transform  
126 spectrometer designed to measure the thermal infrared emission of the Earth-atmosphere system  
127 between 645 and 2760 cm<sup>-1</sup>. Measurements are taken from the polar sun-synchronous orbiting  
128 meteorological Metop series of satellites, every 50 km along the track of the satellite at nadir and  
129 over a swath of 2200 km across track. With more than 14 orbits a day and a field of view of four  
130 simultaneous footprints of 12 km at nadir, IASI provides global coverage of the Earth twice a  
131 day at about 09:30 AM and PM mean local solar time.

132

133 The Metop program consists of a series of three identical satellites successively launched to  
134 ensure homogenous measurements of atmospheric parameters covering more than 15 years.  
135 Metop-A and -B have been successively launched in October 2006 and September 2012,  
136 respectively. The third and last satellite was launched in November 2018 onboard Metop-C. In  
137 addition to its exceptional spatio-temporal coverage, IASI also provides good spectral resolution  
138 and low radiometric noise, which allows the measurement of a series of gas-phase species and  
139 aerosols globally (e.g. Clerbaux et al., 2009; Hilton et al., 2012; Clarisse et al., 2018).

140

141 In this study, we use the O<sub>3</sub> profiles retrieved by the Fast Optimal Retrievals on Layers for IASI  
142 (FORLI-O<sub>3</sub>; version 20151001) near-real time processing chain set up at ULB (See Hurtmans et  
143 al, 2012 for a description of the retrieval parameters and the FORLI performances). The FORLI  
144 algorithm relies on a fast radiative transfer and a retrieval methodology based on the Optimal  
145 Estimation Method (Rodgers, 2000) that requires a priori information (a priori profile and  
146 associated variance-covariance matrix). The FORLI-O<sub>3</sub> a priori consists of one single profile and  
147 one covariance matrix built from the global Logan/Labow/McPeters climatology (McPeters et  
148 al., 2007). The profiles are retrieved on a uniform 1 km vertical grid on 41 layers from surface to  
149 40 km with an extra layer from 40 km to the top of the atmosphere considered at 60 km. Previous  
150 characterization of the FORLI-O<sub>3</sub> profiles (Wespes et al., 2016) have demonstrated a good  
151 vertical sensitivity of IASI to the O<sub>3</sub> measurement with up to 4 independent levels of information  
152 on the vertical profile in the troposphere and the stratosphere (MUS<sub>t</sub>; LSt; upper troposphere-  
153 lower stratosphere – UTLS – 300-150 hPa; middle-low troposphere – MLT – below 300 hPa).  
154 The two stratospheric layers that show distinctive patterns of O<sub>3</sub> distributions over the IASI  
155 decade (Fig. 1a) are characterized by high sensitivity (DOFS > 0.85; Fig. 1b) and low total  
156 retrieval errors (<5%; see Hurtmans et al., 2012; Wespes et al., 2016). The decorrelation between  
157 the MUS<sub>t</sub> and the LSt is further evidenced in Fig. 1d that shows low correlation coefficients (<



158 0.4) between the mean absolute deseasonalized anomalies (as calculated in Wespes et al., 2017)  
159 in the two layers (Fig. 1c). Note that the highest correlation coefficients over the Antarctic (~0.4)  
160 are due to the smaller vertical sensitivity of the IASI measurements over cold surface (Clerbaux  
161 et al., 2009). The latest validation exercises for the FORLI-O<sub>3</sub> product have demonstrated a high  
162 degree of precision with excellent consistency between the measurements taken from the two  
163 IASI instruments on Metop-A and -B, as well as a good degree of accuracy with biases lower  
164 than 20% in the stratospheric layers (Boynard et al., 2018; Keppens et al. 2017). Thanks to these  
165 good IASI-FORLI performances, large-scale dynamical modes of O<sub>3</sub> variations and long-term O<sub>3</sub>  
166 changes can be differentiated in the four retrieved layers (Wespes et al., 2016). The recent  
167 validations have, however, reported a drift in the MUST FORLI-O<sub>3</sub> time series from comparison  
168 with O<sub>3</sub> sondes in the northern hemisphere (N.H.) ( $\sim 3.53 \pm 3.09$  DU.decade<sup>-1</sup> on average over  
169 2008–2016; Boynard et al., 2018) that was suggested to result from a pronounced discontinuity  
170 (“jump”) rather than from a progressive change. Further comparisons with CTM simulations  
171 from the Belgian Assimilation System for Chemical Observations (BASCOE; Chabrillat et al.,  
172 2018; Errera et al., 2019) confirm this jump that occurred on 15 September 2010 over all  
173 latitudes (see Fig. S1 of the supplementary materials). The discontinuity is suspected to result  
174 from updates in level-2 temperature data from Eumetsat that are used as inputs into FORLI (see  
175 Hurtmans et al., 2012). Hence, the apparent drift reported by Boynard et al. (2018) likely results  
176 from the jump rather than from a progressive “instrumental” drift. This is verified by the absence  
177 of drift in the O<sub>3</sub> time series after the jump (non-significant drift of  $-0.38 \pm 2.24$  DU.decade<sup>-1</sup> on  
178 average over October 2010 – May 2017; adapted from Boynard et al., 2018). This is in line with  
179 the excellent stability of the IASI Level-1 radiances over the full IASI period (Buffet et al.,  
180 2016). From the IASI-BASCOE comparisons, the amplitude of the jump has been estimated as  
181 lower than 2.0 DU in the 55°S–55°N latitude band and 4.0 DU in the 55°–90° latitude band of  
182 each hemisphere. The estimated amplitude of the jump is found to be relatively small in  
183 comparison to that of the decadal trends derived in Section 4, hence, it cannot explain the trend  
184 observed in the IASI dataset. Therefore, the jump is not taken into account in the MLR. The  
185 jump values will be, however, considered in the discussion of the O<sub>3</sub> trends (Section 4).

186

187 Finally, the present study only uses the daytime measurements (defined with a solar zenith angle  
188 to the sun < 83°) from the IASI-A (aboard Metop-A) instrument that fully covers the first decade  
189 of the IASI mission. The daytime measurements are characterized by a higher vertical sensitivity  
190 (e.g. Clerbaux et al., 2009). Quality flags developed in previous IASI studies (e.g. Boynard et al.,  
191 2018) were applied a posteriori to exclude data with a poor spectral fit, with less reliability or  
192 with cloud contamination.

193

## 194 **2.2 Multivariate regression model**

195

196 In an effort to unambiguously discriminate anthropogenic trends in O<sub>3</sub> levels from the various  
197 modes of natural variability (illustrated globally in Fig.1c as deseasonalized anomalies), we have

198 applied to the 2.5°x2.5° gridded daily MUST and LSt O<sub>3</sub> time series, a MLR model that is similar  
 199 to that previously developed for tropospheric O<sub>3</sub> studies from IASI (see Wespes et al., 2017;  
 200 2018) but here adapted to fit the stratospheric variations:  
 201

$$202 \quad O_3(t) = Cst + x_{j=1} \cdot trend + \sum_{n=1,2} [a_n \cdot \cos(n\omega t) + b_n \cdot \sin(n\omega t)] + \sum_{j=2}^m x_j X_{norm,j}(t) + \varepsilon(t) \quad (1)$$

203  
 204 where  $t$  is the number of days,  $x_1$  is the trend coefficient in the data,  $\omega = 2\pi/365.25$ ,  $a_n, b_n, x_j$  are  
 205 the regression coefficients of the seasonal and non-seasonal variables and  $\varepsilon(t)$  is the residual  
 206 variation (assumed to be autoregressive with time lag of 1 day).  $X_{norm,j}$  are the  $m$  chosen  
 207 explanatory variables, commonly called “proxies”, which are normalized over the study period  
 208 (2008 – 2017) with:  
 209

$$210 \quad X_{norm}(t) = 2[X(t) - X_{median}] / [X_{max} - X_{min}] \quad (2)$$

211  
 212 In addition to harmonic terms that represent the 1-yr and 6-month variations, the MLR model  
 213 includes the anthropogenic O<sub>3</sub> response through a linear trend (LT) term and a set of proxies to  
 214 parameterize the geophysical processes influencing the abundance of O<sub>3</sub> in the stratosphere. The  
 215 MLR uses an iterative stepwise backward elimination approach to retain, at the end of the  
 216 iterations, the most relevant proxies (with a 95% confidence level) explaining the O<sub>3</sub> variations  
 217 (e.g. Mäder et al., 2007). Table 1 lists the selected proxies, their sources and their temporal  
 218 resolutions. The proxies describe the influence of the Quasi-Biennial Oscillation (QBO; visible  
 219 from the deseasonalized anomaly maps in Fig.1c with a typical band-like pattern around the  
 220 Equator) at 10 hPa and 30 hPa, of the North Atlantic and the Antarctic Oscillations (NAO and  
 221 AAO), of the El Niño/Southern Oscillation (ENSO), of the volcanic aerosols (AERO) injected  
 222 into the stratosphere, of the strength of the Brewer-Dobson circulation (BDC) with the Eliassen-  
 223 Palm flux (EPF), of the polar O<sub>3</sub> loss driven by the volume of polar stratospheric clouds (VPSC),  
 224 of the tropopause height variation with the geopotential height (GEO) and of the mixing of  
 225 tropospheric and stratospheric air masses with the potential vorticity (PV). The main proxies in  
 226 terms of their influence on O<sub>3</sub> are illustrated in Fig. 2 over the period of the IASI mission. The  
 227 construction of the EPF, VPSC and AERO proxies, which are specifically used in this study, is  
 228 explained hereafter, while the description of the other proxies can be found in previous IASI  
 229 studies (Wespes et al., 2016; Wespes et al., 2017).  
 230

231 The EPF proxy consists of the normalized upward component of the EP flux crossing 100 hPa  
 232 and spatially averaged over the 45°-75° latitude band for each hemisphere. The fluxes are  
 233 calculated from the NCEP/NCAR 2.5°x2.5° gridded daily reanalysis (Kalnay et al., 1996) over  
 234 the IASI decade. The VPSC proxy is based on the potential volume of PSCs given by the volume

235 of air below the formation temperature of nitric acid trihydrate (NAT) over 60°-90° north and  
236 south and calculated from the ERA-Interim reanalysis and from the MLS climatology of nitric  
237 acid (I. Wohltmann, private communication; Wohltmann et al., 2007; and references therein).  
238 The PSC volume is multiplied by the EESC to account for the changes in the amount of  
239 inorganic stratospheric chlorine that activates the polar ozone loss. The O<sub>3</sub> build-up and the polar  
240 O<sub>3</sub> loss are highly correlated with wintertime accumulated EP flux and PSC volume, respectively  
241 (Fusco and Salby, 1999; Randel et al., 2002; Fioletov and Shepherd, 2003 and Rex et al., 2004).  
242 These cumulative EP flux and PSC effects on O<sub>3</sub> levels are taken into account by integrating the  
243 EPF and VPSC proxies over time with a specific exponential decay time according to the  
244 formalism of Brunner et al. (2006; see Eq. 4). We set the relaxation time scale to 3 months  
245 everywhere, except during the wintertime build-up phase of O<sub>3</sub> in the extratropics (from October  
246 to March in the N.H. and from April to September in the southern hemisphere - S.H.) when it is  
247 set to 12 months. For EPF, it accounts for the slower relaxation time of extratropical O<sub>3</sub> in winter  
248 due to its longer photochemical lifetime. For VPSC, the 12-month relaxation time accounts for a  
249 stronger effect of stratospheric chlorine on spring O<sub>3</sub> levels: the maximum of the accumulated  
250 VPSC (Fig. 2) coincides with the maximum extent of O<sub>3</sub> hole that develops during springtime  
251 and that lasts until November. Note that correlations between VPSC and EPF are possible since  
252 the same method is used to build these cumulative proxies. VPSC and EPF are also dynamically  
253 anti-correlated to some extent since a strong BDC is connected with warm polar stratospheric  
254 temperatures and, hence, reduced PSC volume (e.g. Wohltmann et al., 2007).

255  
256 The AERO proxy is derived from aerosol optical depth (AOD) of sulfuric acid only. That proxy  
257 consists of latitudinally averaged (22.5°N-90°N – AERO-N, 22.5°S-90°S – AERO-S and 22.5°S-  
258 22.5°N – AERO-Eq) extinction coefficients at 12 μm calculated from merged aerosol datasets  
259 (SAGE, SAM, CALIPSO, OSIRIS, 2D-model-simulation and Photometer; Thomason et al.,  
260 2018) and vertically integrated over the two IASI stratospheric O<sub>3</sub> columns (AERO-MUST and  
261 AERO-LSt). Fig.2 shows the AERO proxies (AERO-N, AERO-S and AERO-Eq) corresponding  
262 to the AOD over the whole stratosphere (150-2 hPa), while Fig.3 represents the latitudinal  
263 distribution of the volcanic sulfuric acid extinction coefficients integrated over the whole  
264 stratosphere (top panel) and, separately, over the MUST (middle panel) and the LSt (bottom  
265 panel) from 2005 to 2017. The AOD distributions indicate the need for considering one specific  
266 AERO proxy for each latitudinal band (AERO-N, AERO-S and AERO-Eq) and for each vertical  
267 layer (AERO-MUST and AERO-LSt). Note that, as an alternative proxy to AERO, the surface  
268 area density of ambient aerosol, that represents the aerosol surface available for chemical  
269 reactions, has been tested, giving similar results.

270  
271 Note also that, similarly to what has already been found for tropospheric O<sub>3</sub> from IASI (Wespes  
272 et al., 2016), several time-lags for ENSO (1-, 3- and 5-month lags; namely, ENSO-lag1, ENSO-  
273 lag3 and ENSO-lag5) are also included in the MLR model to account for a possible delay in the  
274 O<sub>3</sub> response to ENSO at high latitudes.

275  
 276 Finally, autocorrelation in the noise residual  $\varepsilon(t)$  (see Eq. 1 in Wespes et al., 2016) is accounted  
 277 for in the MLR analysis with time lag of one day to yield the correct estimated standard errors  
 278 for the regression coefficients. They are estimated from the covariance matrix of the regression  
 279 coefficients and corrected at the end of the iterative process by the autocorrelation of the noise  
 280 residual. The regression coefficients are considered significant if they fall in the 95% confidence  
 281 level (defined by  $2\sigma$  level).

282  
 283 In the seasonal formulation of the MLR model, the main proxies ( $x_j X_{norm,j}$ ; with  $x_j$ , the  
 284 regression coefficient and  $X_{norm,j}$ , the normalized proxy) are split into four seasonal functions  
 285 ( $x_{spr} X_{norm,spr} + x_{sum} X_{norm,sum} + x_{fall} X_{norm,fall} + x_{wint} X_{norm,wint}$ ) that are independently and  
 286 simultaneously adjusted for each grid cell (Wespes et al., 2017). Hence, the seasonal MLR  
 287 adjusts 4 coefficients (instead of one in the annual MLR) to account for the seasonal O<sub>3</sub> response  
 288 to changes in the proxy. If that method avoids to over-constrain the adjustment by the year-round  
 289 proxies and, hence, reduces the systematic errors, the smaller daily data points covered by the  
 290 seasonal proxies translate to a lower significance of these proxies. This is particularly true for  
 291 EPF and VPSC that compensate each other by construction. As a consequence, the annual MLR  
 292 is performed first in this study and, then, complemented with the seasonal one when it is found  
 293 helpful for further interpreting the observations.

294  
 295 Figure 4 shows the latitudinal distributions of the O<sub>3</sub> columns in the two stratospheric layers over  
 296 the IASI decade (first panels in Fig.4 a and b), as well as those simulated by the annual MLR  
 297 regression model (second panels) along with the regression residuals (third panels). The root  
 298 mean square error (*RMSE*) of the regression residual and the contribution of the MLR model into  
 299 the IASI O<sub>3</sub> variations (calculated as  $\frac{\sigma(O_3^{\text{Fitted\_model}}(t))}{\sigma(O_3(t))}$  where  $\sigma$  is the standard deviation relative

300 to the regression model and to the IASI time series; bottom panels) are also represented (bottom  
 301 panels). The results indicate that the model reproduces ~25-85% and ~35-95% of the daily O<sub>3</sub>  
 302 variations captured by IASI in the MUST and the LSt, respectively, with the best representation  
 303 in the tropics and the worst around the S.H. polar vortex, and that the residual errors are  
 304 generally lower than 10% everywhere for the two layers, except for the spring O<sub>3</sub> hole region in  
 305 the LSt. The *RMSE* relative to the IASI O<sub>3</sub> time series are lower than 15 DU and 20 DU at global  
 306 scale in the MUST and the LSt, respectively, except around the S.H. polar vortex in the LSt (~30  
 307 DU). On a seasonal basis (figure not shown), the results are only slightly improved: the model  
 308 explains from ~35-90% and ~45-95% of the annual variations and the *RMSE* are lower than ~12  
 309 DU and ~23 DU everywhere, in the MUST and the LSt, respectively. These results verify that the  
 310 MLR models (annual and seasonal) reproduce well the time evolution of O<sub>3</sub> over the IASI

311 decade in the two stratospheric layers and, hence, that they can be used to identify and quantify  
312 the main O<sub>3</sub> drivers in these two layers (see Section 3).

313

314 The MLR model has also been tested on nighttime FORLI-O<sub>3</sub> measurements only and  
315 simultaneously with daytime measurements, but this resulted in a lower quality fit, especially in  
316 the MUST over the polar regions. This is due to the smaller vertical sensitivity of IASI during  
317 nighttime measurements, especially over cold surface, which causes larger correlations between  
318 stratospheric and tropospheric layers (e.g. 40-60% at high northern latitudes versus ~10-20% for  
319 daytime measurements based on deseasonalized anomalies) and, hence, which mixes  
320 counteracting processes from these two layers. For this reason, only the results for the MLR  
321 performed on daytime measurements are presented in this paper.

322

### 323 **3 Drivers of O<sub>3</sub> natural variations**

324

325 Ascribing a recovery in stratospheric O<sub>3</sub> to a decline in stratospheric halogen species requires  
326 first identifying and quantifying natural cycles that may produce trend-like segments in the O<sub>3</sub>  
327 time series, in order to prevent any misinterpretation of those segments as signs of O<sub>3</sub> recovery.  
328 The MLR analysis performed in Section 2.2 that was found to give a good representation of the  
329 MUST and LSt O<sub>3</sub> records shows distinctive relevant patterns for the individual proxies retained  
330 in the regression procedure, as represented in Fig. 5. The fitted drivers are characterized by  
331 significant regional differences in their regression coefficients with regions of in-phase relation  
332 (positive coefficients) or out-of-phase relation (negative coefficients) with respect to the IASI  
333 stratospheric O<sub>3</sub> anomalies. The areas of significant drivers (in the 95% confidence limit) are  
334 surrounded by non-significant cells when accounting for the autocorrelation in the noise residual.  
335 Figures 6 a and b, respectively, represent the latitudinal averages of the fitted regression  
336 coefficients for the significant proxies showing latitudinal variation only in the O<sub>3</sub> response  
337 (namely, QBO, EPF, VPSC, AERO and ENSO) and of the contribution of these drivers into the  
338 O<sub>3</sub> variability (calculated as the product of the 2 $\sigma$  variability of each proxy by its corresponding  
339 fitted coefficient, i.e. the 2 $\sigma$  variability of the reconstructed proxies). The 2 $\sigma$  O<sub>3</sub> variability in the  
340 IASI measurements and in the fitted MLR model are also represented (black and grey lines,  
341 respectively). Figure 7 displays the same results as Fig. 6b but for the austral spring and winter  
342 periods only (using the seasonal MLR).

343

344 The PV and GEO proxies are generally minor components (not shown here) with relative  
345 contributions smaller than 10% and large standard errors (>80%), except in the tropics where the  
346 contribution for GEO reaches 40% in the LSt due to the tropopause height variation. Each other  
347 adjusted proxy (QBO, SF, EPF, VPSC, AERO, ENSO, NAO and AAO) is an important  
348 contributor to the O<sub>3</sub> variations, depending on the layer, region, and season as described next:

349

- 350 1. QBO - The QBO at 10hPa and 30hPa are important contributors around the Equator for  
351 the two stratospheric layers. It shows up as a typical band-like pattern of high positive  
352 coefficients confined equatorward of  $\sim 15^\circ\text{N/S}$  where the QBO is known to be a dominant  
353 dynamical modulation force associated to strong convective anomalies (e.g. Randel and  
354 Wu, 1996; Tian et al., 2006; Witte et al., 2008). In that latitude band, QBO10 and QBO30  
355 explain up to  $\sim 8$  DU and  $\sim 5$  DU, respectively, of the MUST and LSt yearly  $\text{O}_3$  variations  
356 (see Fig. 5 and 6b; i.e. relative contributions up to  $\sim 50\%$  and  $\sim 40\%$  for QBO10/30 in  
357 MUST and LSt  $\text{O}_3$ , respectively). The QBO is also influencing  $\text{O}_3$  variations poleward of  
358  $60^\circ\text{N/S}$  with a weaker correlation between  $\text{O}_3$  and equatorial wind anomalies as well as in  
359 the sub-tropics with an out-of-phase transition. That pole-to-pole QBO influence results  
360 from the QBO-modulation of extra-tropical waves and its interaction with the BDC (e.g.  
361 Fusco and Salby, 1999). A pronounced seasonal dependence is observed in the out-of-  
362 phase sub-tropical  $\text{O}_3$  anomalies in the MUST, with the highest amplitude oscillating  
363 between the hemispheres in their respective winter ( $\sim 5$  DU of  $\text{O}_3$  variations explained by  
364 QBO10/30 at  $\sim 20^\circ\text{S}$  during JJA and at  $\sim 20^\circ\text{N}$  during DJF; see Fig. 7b for the JJA period  
365 in the MUST the DJF period is not shown), which is in agreement with Randel and Wu  
366 (1996). The amplitude of the QBO signal is found to be stronger for QBO30 than for  
367 QBO10 in the LSt, which is in good agreement with studies from other instruments for  
368 the total  $\text{O}_3$  (e.g. Baldwin et al., 2001; Steinbrecht et al., 2006; Frossard et al., 2013;  
369 Coldewey-Egbers et al., 2014) and from IASI in the troposphere (Wespes et al., 2017).  
370 The smaller amplitude of  $\text{O}_3$  response to QBO10 in the LSt compared to the MUST is  
371 again in agreement with previous studies that reported changes in phase of the QBO10  
372 response as a function of altitude with a positive response in the upper stratosphere and  
373 destructive interference in the mid-low stratosphere (Chipperfield et al., 1994; Brunner et  
374 al., 2006).
- 375
- 376 2. SF - In the MUST layer, the solar cycle  $\text{O}_3$  response is one of the strongest contributors  
377 and explains globally between  $\sim 2$  and 15 DU of in-phase  $\text{O}_3$  variations (i.e. higher  $\text{O}_3$   
378 values during maximum solar irradiance) with the largest amplitude over the highest  
379 latitude regions (see Fig. 5; relative contribution up to  $\sim 20\%$ ). The solar influence in LSt  
380 is more complex with regions of in-phase and out-of-phase  $\text{O}_3$  variations. The impact of  
381 solar variability on stratospheric  $\text{O}_3$  abundance is due to a combination of processes: a  
382 modification in the  $\text{O}_3$  production rates in the upper stratosphere induced by changes in  
383 spectral solar irradiance (e.g. Brasseur et al., 1993), the transport of solar proton event-  
384 produced  $\text{NO}_y$  from the mesosphere down to the mid-low stratosphere where it decreases  
385 active chlorine and bromine and, hence,  $\text{O}_3$  destruction (e.g. Jackman et al., 2000; Hood  
386 and Soukharev, 2006; and references therein) while it enhances the  $\text{O}_3$  destruction in the  
387 MUST through  $\text{NO}_x$  catalysed cycles, and its impact on the lower stratospheric dynamics  
388 including the QBO (e.g. Hood et al., 1997; Zerefos et al., 1997; Kodera and Kuroda,  
389 2002; Hood and Soukharev, 2003, Soukharev and Hood, 2006). As for the QBO, the

390 strong SF dependence at polar latitudes in the LSt with zonal asymmetry in the O<sub>3</sub>  
391 response reflects the influence of the polar vortex strength and of stratospheric warmings,  
392 and are in good agreement with previous results (e.g. Hood et al., 1997; Zerefos et al.,  
393 1997; Labitzke and van Loon, 1999; Steinbrecht et al., 2003; Coldewey-Egbers et al.,  
394 2014). It is also worth noting that because only one solar cycle is covered, the QBO and  
395 SF effects could not be completely separated because of their strong interaction (e.g.  
396 McCormack et al., 2007; Roscoe et al., 2007; Kuttippurath et al., 2013).

397

398 3. EPF - The vertical component of the planetary wave Eliassen-Palm flux entering the  
399 lower stratosphere corresponds to the divergence of the wave momentum that drives the  
400 meridional residual Brewer-Dobson circulation. In agreement with previous studies (e.g.  
401 Fusco and Salby, 1999; Randel et al., 2002; Brunner et al., 2006; Weber et al., 2011),  
402 fluctuations in the BDC are shown to cause changes on stratospheric O<sub>3</sub> distribution  
403 observed from IASI: EPF largely positively contributes to the LSt O<sub>3</sub> variations at high  
404 latitudes of both hemispheres where O<sub>3</sub> is accumulated because of its long chemical  
405 lifetime, with amplitude ranging between ~20 and 100 DU (see Fig. 5 and 6; i.e. relative  
406 contribution of ~35-150%). The influence of the EPF decreases at lower latitudes where a  
407 stronger circulation induces more O<sub>3</sub> transported from the tropics to middle-high latitudes  
408 and, hence, a decrease in O<sub>3</sub> levels particularly below 20 km (Brunner et al., 2006). The  
409 influence of EP fluxes in the Arctic is the smallest in summer (see Fig.7; <~35 DU vs ~70  
410 DU in fall; the two other seasons are not shown) due to the later O<sub>3</sub> build-up in polar  
411 vortices. In the S.H., because of the formation of the O<sub>3</sub> hole, the EP influence is smaller  
412 than in the N.H. and the seasonal variations are less marked. In the MUST, the O<sub>3</sub>  
413 response attributed to variations in EPF is positive in both hemispheres, with a much  
414 lower amplitude than in the LSt (up to ~20-35 DU). The region of out-of-phase relation  
415 with negative EPF coefficients over the high southern latitudes (Fig. 5b) is likely  
416 attributable to the influence of VPSC that has correlations with EPF by construction (see  
417 Section 2.2). Furthermore, given the annual oscillations in EPF, compensation by the 1-yr  
418 harmonic term (eq. 1, Section 2) is found, but it remains weaker than the EPF  
419 contribution (data not shown), in particular at high latitudes where the EPF contribution  
420 is the largest.

421

422 4. VPSC - Identically to EPF, VPSC is shown to mainly contribute to O<sub>3</sub> variations in LSt  
423 over the polar regions (~55 DU or 40% in the N.H. vs ~60 DU or 85% in the S.H. on a  
424 longitudinal average; see Fig. 6b) but with an opposite phase (Fig. 5 and 6a). The  
425 amplitude of the O<sub>3</sub> response to VPSC reaches its maximum over the southern latitudes  
426 during the spring (~60 DU; see Fig.7a for the austral spring period), which is consistent  
427 with the role of PSCs on the polar O<sub>3</sub> depletion when there is sufficient sunlight. The  
428 strong VPSC influence found at high northern latitudes in fall (Fig. 7a) are due to  
429 compensation effects with EPF as pointed out above and verified from sensitivity tests

430 (not shown). Note also that the VPSC contribution into MUST reflects the larger  
431 correlation between the two stratospheric layers over the southern polar region (Section  
432 2.1, Fig. 1d).

433  
434 5. AERO - Five important volcanic eruptions with stratospheric impact occurred during the  
435 IASI mission (Kasatochi in 2008, Sarychev in 2009, Nabro in 2011, Sinabung in 2014  
436 and Calbuco in 2015; see Fig.3). The two major eruptions of the last decades, El Chichon  
437 (1982) and Mt. Pinatubo (1991) have injected sulfur gases into the stratosphere. They  
438 have been shown to enhance PSCs particle abundances (~15-25 km altitude), to remove  
439 NO<sub>x</sub> (through reaction with the surface of the sulfuric aerosol to form nitric acid) and,  
440 hence, to make the ozone layer more sensitive to active chlorine (e.g. Hofmann et al.,  
441 1989; Hofmann et al., 1993; Portmann et al., 1996; Solomon et al., 2016). Besides this  
442 chemical effect, the volcanic aerosols also warm the stratosphere at lower latitudes  
443 through scattering and absorption of solar radiation, which further induces indirect  
444 dynamical effects (Dhomse et al., 2015; Revell et al., 2017). Even though the recent  
445 eruptions have been of smaller magnitude than El Chichon and Mt. Pinatubo, they  
446 produced sulphur ejection through the tropopause into the stratosphere (see Section 2.2,  
447 Fig.2 and Fig.3), as seen with AOD reaching  $5 \times 10^{-4}$  over the stratosphere (150-2 hPa),  
448 especially following the eruptions of Nabro (13.3°N, 41.6°E), Sinabung (3.1°N, 98.3°E)  
449 and Calbuco (41.3°S, 72.6°W). In the LSt, the regression supports an enhanced O<sub>3</sub>  
450 depletion over the Antarctic in presence of sulfur gases with a significantly negative  
451 annual O<sub>3</sub> response reaching ~25 DU (i.e. relative contribution of ~20% into O<sub>3</sub> variation;  
452 see Fig. 5b). On the contrary, enhanced O<sub>3</sub> levels in response to sulfuric acid are found in  
453 the MUST with a maximum impact of up to 10 DU (i.e. relative contribution of ~20% into  
454 the O<sub>3</sub> variation; see Fig. 5a) over the Antarctic. The change in phase in the O<sub>3</sub> response  
455 to AERO between the LSt (~15-25 km) and the MUST (~25-40 km) over the Antarctic, as  
456 well as between polar and lower latitudes in the LSt (see Fig.5 and 6a), agree well with  
457 the heterogeneous reactions on sulfuric aerosol surface, which reduce the concentration  
458 of NO<sub>x</sub> to form nitric acid, leading to enhanced O<sub>3</sub> levels above 25 km but leading to  
459 decreased O<sub>3</sub> levels due to chlorine activation below 25 km (e.g. Solomon et al., 1996).  
460 On a seasonal basis, the depletion due to the presence of sulfur gases reaches ~30 DU on  
461 a longitudinal average, over the S.H. polar region during the austral spring (see Fig.7a)  
462 highlighting the link between volcanic gases converted to sulfate aerosols and  
463 heterogeneous polar halogen chemistry.

464  
465 6. NAO – The NAO is an important mode of global climate variability, particularly in  
466 northern winter. It describes large-scale anomalies in sea level pressure systems between  
467 the sub-tropical Atlantic (Azores; high pressure system) and sub-polar (Iceland; low  
468 pressure system) regions (Hurrell, 1995). It disturbs the location and intensity of the  
469 North Atlantic jet stream that separates these two regions depending on the phase of



470 NAO. The positive (negative) phase of the NAO corresponds to larger (weaker) pressure  
471 difference between the two regions leading to stronger westerlies (easterlies) across the  
472 mid-latitudes (Barnston and Livezey, 1987). The two pressure system regions are clearly  
473 identified in the stratospheric O<sub>3</sub> response to NAO, particularly in the LSt, with positive  
474 regression coefficients above the Labrador-Greenland region and negative coefficients  
475 above the Euro-Atlantic region (Fig. 5b). Above these two sectors, the positive phase  
476 induces, respectively, an increase and a decrease in LSt O<sub>3</sub> levels. The negative phase is  
477 characterized by the opposite behaviour. That NAO pattern is in line with previous  
478 studies (Rieder et al., 2013) and was also observed from IASI in tropospheric O<sub>3</sub> (Wespes  
479 et al., 2017). The magnitude of annual LSt O<sub>3</sub> changes attributed to NAO variations  
480 reaches ~20 DU over the in-phase Labrador region (i.e. contribution of 25% relative to  
481 the O<sub>3</sub> variations), while a much lower contribution is found for the MUST (~4 DU or  
482 ~10%). The NAO coefficient in the LSt also shows that the influence of the NAO  
483 extends further into northern Asia in the case of prolonged NAO phases. The NAO has  
484 also been shown to influence the propagation of waves into the stratosphere, hence, the  
485 BDC and the strength of the polar vortex in the N.H. mid-winter (Thompson and  
486 Wallace, 2000; Schnadt and Dameris, 2003; Rind et al., 2005). That connection between  
487 the NAO and the BDC might explain the negative anomaly in the O<sub>3</sub> response to EPF in  
488 the LSt over northern Asia that matches the region of negative response to the NAO.

- 489
- 490 7. AAO - The extra-tropical circulation of the S.H. is driven by the Antarctic oscillation that  
491 is characterized by geopotential height anomalies south of 20°S, with high anomalies of  
492 one sign centered in the polar region and weaker anomalies of the opposing sign north of  
493 55°S (Thompson and Wallace, 2000). This corresponds well to the two band-like regions  
494 of opposite signs found for the regression coefficients of adjusted AAO in the LSt  
495 (negative coefficients centered in Antarctica and positive coefficient north of ~40°S; see  
496 Fig.5b). Similarly to the NAO, the strength of the residual mean circulation and of the  
497 polar vortex in the S.H. are modulated by the AAO through the atmospheric wave  
498 activity (Thompson and Wallace, 2000; Thompson and Solomon, 2001). During the  
499 positive (negative) phase of the AAO, the BDC is weaker (stronger) leading to less  
500 (more) O<sub>3</sub> transported from the tropics into the southern polar region, and the polar  
501 vortex is stronger (weaker) leading to more (less) O<sub>3</sub> depletion inside. This likely  
502 explains both the positive AAO coefficients in the region north of ~40°S (contribution <  
503 ~5 DU or ~10%) and the negative coefficients around and over the Antarctic  
504 (contribution reaching ~10 DU or ~15%; exception is found with positive coefficients  
505 over the western Antarctic). The dependence of O<sub>3</sub> variations to the AAO in the MUST is  
506 lower than ~7 DU (or ~15%).
- 507
- 508 8. ENSO - Besides the NAO and the AAO, the El Nino southern oscillation is another  
509 dominant mode of global climate variability. This coupled ocean-atmosphere

510 phenomenon is governed by sea surface temperature (SST) differences between high  
511 tropical and low extra-tropical Pacific regions (Harrison and Larkin, 1998). Domeisen et  
512 al. (2019) have recently reviewed the possible mechanisms connecting the ENSO to the  
513 stratosphere in the tropics and the extratropics of both hemispheres. The ozone response  
514 to ENSO is represented in Fig. 5 only for the ENSO-lag3 proxy which is found to be the  
515 main ENSO proxy contributing to the observed O<sub>3</sub> variations. While in the troposphere,  
516 previous works have shown that the ENSO influence mainly results in a high contrast of  
517 the regression coefficients between western Pacific/Indonesia/North Australia and  
518 central/eastern Pacific regions caused by reduced rainfalls and enhanced O<sub>3</sub> precursor  
519 emissions above western Pacific (called “chemical effect”) (e.g. e.g. Oman et al., 2013;  
520 Valks et al., 2014; Ziemke et al., 2015; Wespes et al., 2016; and references therein), the  
521 LSt O<sub>3</sub> response to ENSO is shown here to translate into a strong tropical-extratropical  
522 gradient in the regression coefficients with a negative response in the tropics and a  
523 positive response at higher latitudes (~5 DU and ~10 DU, respectively, on longitudinal  
524 averages; see Fig. 6a). In the MUST, ENSO is globally a smaller out-of-phase driver of O<sub>3</sub>  
525 variations (response of ~5 DU). The decrease in LSt O<sub>3</sub> during the warm ENSO phase in  
526 the tropics (characterized by a negative ENSO lag-3 coefficient reaching 7 DU (or 35%),  
527 respectively, in the LSt; see Fig. 5) is consistent with the ENSO-modulated upwelling via  
528 deep convection in the tropical lower stratosphere and, hence, increased BD circulation  
529 (e.g. Randel et al., 2009). The in-phase accumulation of LSt O<sub>3</sub> in the extra-tropics  
530 (contribution reaching 15 DU or 20%; see Fig. 5) is also consistent with enhanced extra-  
531 tropical planetary waves that propagate into the stratosphere during the warm ENSO  
532 phase, resulting in sudden stratospheric warmings and, hence, in enhanced BDC and  
533 weaker polar vortices (e.g. Brönnimann et al., 2004; Manzini et al., 2006; Cagnazzo et  
534 al., 2009). The very pronounced link between stratospheric O<sub>3</sub> and the ENSO related  
535 dynamical pathways with a time lag of about 3 months is one key finding of the present  
536 work. Indeed, the influence of ENSO on stratospheric O<sub>3</sub> measurements has already been  
537 reported in earlier studies (Randel and Cobb, 1994; Brönnimann et al., 2004; Randel et  
538 al., 2009; Randel and Thompson, 2011; Oman et al., 2013; Manatsa and Mukwada, 2017;  
539 Tweedy et al., 2018), but it is the first time that a delayed stratospheric O<sub>3</sub> response is  
540 investigated in MLR studies. A 4- to 6-month time lag in O<sub>3</sub> response to ENSO has  
541 similarly been identified from IASI in the troposphere (Wespes et al., 2017), where it was  
542 explained not only by a tropospheric pathway but also by a specific stratospheric pathway  
543 similar to that modulating stratospheric O<sub>3</sub> but with further impact downward onto  
544 tropospheric circulation (Butler et al., 2014; Domeisen et al., 2019). Furthermore, the 3-  
545 month lag identified in the LSt O<sub>3</sub> response is fully consistent with the modelling work of  
546 Cagnazzo et al. (2009) that reports a warming of the polar vortex in February-March  
547 following a strong ENSO event (peak activity in November-December) associated with  
548 positive O<sub>3</sub> ENSO anomaly reaching ~10 DU in the Arctic and negative anomaly of ~6-7  
549 DU in the Tropics. We find that the tropical-extra-tropical gradient in O<sub>3</sub> response to

550 ENSO-lag3 is indeed much stronger in spring with contributions of ~20-30 DU (see  
551 Fig.7a for the austral spring period vs winter).

552  
553 Overall, although the annual MLR model underestimates the O<sub>3</sub> variability at high latitudes  
554 (>50°N/S) by up to 5 DU, particularly in the MUST (see Fig. 6b), we conclude that it gives a  
555 good overall representation of the sources of O<sub>3</sub> variability in the two stratospheric layers  
556 sounded by IASI. This is particularly true for the spring period (see Fig. 7) which was studied in  
557 several earlier works to reveal the onset of Antarctic total O<sub>3</sub> recovery (Salby et al., 2011;  
558 Kuttippurath et al., 2013; Shepherd et al., 2014; Solomon et al., 2016; Weber et al., 2018),  
559 despite the large O<sub>3</sub> variability due to the hole formation during that period (~80 DU; see Fig.7a,  
560 LSt panel). It is also interesting to see from Fig.7 that the broad O<sub>3</sub> depletion over Antarctica in  
561 the LSt is attributed by the MLR to VPSC (up to 60 DU of explained O<sub>3</sub> variability on a  
562 latitudinal average). Following these promising results, we further analyze below the O<sub>3</sub>  
563 variability in response to anthropogenic perturbations, assumed in the MLR model by the linear  
564 trend term, with a focus over the polar regions.

565

## 566 **4 Trend analysis**

567

### 568 **4.1 10-year trend detection in stratospheric layers**

569

570 The distributions of the linear trend estimated by the annual regression are represented in Fig. 8a  
571 for the MUST and the LSt (left and right panels). In agreement with the early signs of O<sub>3</sub>  
572 recovery reported for the extra-tropical mid- and upper stratosphere above ~25-10 hPa (>25-30  
573 km; Pawson et al., 2014; Harris et al., 2015; Steinbrecht et al., 2017; Sofieva et al., 2017; Ball et  
574 al., 2018), the MUST shows significant positive trends larger than 1 DU/yr poleward of ~35°N/S  
575 (except over Antarctica). The corresponding decadal trends (>10 DU/decade) are much larger  
576 than the discontinuity of ~2-4 DU encountered in the MUST record on 15 September 2010 and  
577 discussed in section 2.1. The tropical MUST also shows positive trends but they are weaker (<0.8  
578 DU/yr) or not significant. The largest increase is observed in polar O<sub>3</sub> with amplitudes reaching  
579 ~2.0 DU/yr. The mid-latitudes also show significant O<sub>3</sub> enhancement which can be attributed to  
580 air mass mixing after the disruption of the polar vortex (Knudsen and Grooss, 2000; Fioletov and  
581 Shepherd, 2005; Dhomse, 2006; Nair et al., 2015).

582

583 As in the MUST, the LSt is characterized in the southern polar latitudes by significantly positive  
584 and large trends (between ~ 1.0 and 2.5 DU/yr). In the mid-latitudes, the lower stratospheric  
585 trends are significantly negative, i.e. opposite to those obtained in the MUST. This highlights the  
586 independence between the two O<sub>3</sub> layers sounded by IASI in the stratosphere. Poleward of 25°N  
587 the negative LSt trends range between ~ -0.5 and -1.7 DU/yr. Negative trends in lower  
588 stratospheric O<sub>3</sub> have already been reported in extra-polar regions from other space-based  
589 measurements (Kyrölä et al., 2013; Gebhardt et al., 2014; Sioris et al., 2014; Harris et al., 2015;

590 Nair et al., 2015; Vigouroux et al., 2015; Wespes et al., 2016; Steinbrecht et al., 2017; Ball et al.,  
591 2018) and may be due to changes in stratospheric dynamics at the decadal timescale (Galytska et  
592 al., 2019). These previous studies, which were characterized by large uncertainties or resulted  
593 from composite-data merging techniques, are confirmed here using a single dataset. The negative  
594 trends which are observed at lower stratospheric middle latitudes are difficult to explain with  
595 chemistry-climate models (Ball et al., 2018). It is also worth noting that the significant MUsT and  
596 LSt O<sub>3</sub> trends are of the same order as those previously estimated from IASI over a shorter  
597 period (from 2008 to 2013) and latitudinal averages (see Wespes et al., 2016). This suggests that  
598 the trends are not very sensitive to the natural variability in the IASI time series, hence,  
599 supporting the significance of the O<sub>3</sub> trends presented here.

600  
601 The sensitivity of IASI O<sub>3</sub> to the estimated trend from MLR is further verified in Fig. 8b that  
602 represents the global distributions of relative differences in the *RMSE* of the regression residuals  
603 obtained with and without a linear trend term included in the MLR model ( $(RMSE_{w/o\_LT} -$   
604  $RMSE_{with\_LT})/RMSE_{with\_LT} \times 100$ ; in %). An increase of ~1.0-4.0% and ~0.5-2.0% in the *RMSE*  
605 is indeed observed for both the MUsT and the LSt, respectively, in regions of significant trend  
606 contribution (Fig. 8a), when the trend is excluded. This demonstrates the significance of the  
607 trend in improving the performance of the regression. Another statistical method that can be used  
608 for evaluating the possibility to infer, from the IASI time period, the significant positive or  
609 negative trends in the MUsT and the LSt, respectively, consists in determining the expected year  
610 when these specified trends would be detectable from the available measurements (with a  
611 probability of 90%) by taking into account the variance ( $\sigma_\epsilon^2$ ) and the autocorrelation ( $\Phi$ ) of the  
612 noise residual according to the formalism of Tiao et al. (1990) and Weatherhead et al. (1998).  
613 The 95% confidence interval for that expected trend detection year can also be determined. Such  
614 a method has already been used for evaluating the trends derived from IASI in the troposphere  
615 (Wespes et al., 2018). It represents a more drastic and conservative method than the standard  
616 MLR. The results are displayed in Fig. 8c for an assumed specified trend of |1.5| DU/yr, which  
617 corresponds to a medium amplitude of trends derived here above from the MLR over the mid-  
618 polar regions (Fig. 8a). In the MUsT, we find that ~2-3 additional years of IASI measurements  
619 would be required to unequivocally detect a trend of |1.5| DU/yr (with probability 0.90) over  
620 high latitudes (detectable from ~2020-2022  $\pm$  6-12 months) whereas it should already be  
621 detectable over the mid- and lower latitudes (from ~2015  $\pm$  3-6 months). In the LSt, an additional  
622 ~7 years ( $\pm$  1-2 years) of IASI measurements would be required to categorically identify the  
623 probable decline derived from the MLR in northern mid-latitudes, and even more to measure the  
624 enhancement in the southern polar latitudes. The longer required measurement period at high  
625 latitudes is due to the larger noise residuals in the regression fits (i.e. largest  $\sigma_\epsilon$ ) at these  
626 latitudes (see Fig.4 a and b). Note that a larger specified trend amplitude would obviously require  
627 a shorter period of IASI measurement. We find that only ~2 additional years would be required

628 to detect a specified trend of  $|2.5|$  DU/yr which characterizes the LSt at high latitudes (data not  
629 shown).

630

#### 631 **4.2 Stratospheric contributions to total O<sub>3</sub> trend**

632

633 The effect on total O<sub>3</sub> of the counteracting trends in the northern mid-latitudes and of the  
634 constructive trends in the southern polar latitudes in the two stratospheric layers sounded by IASI  
635 is now investigated.

636

637 Figure 9 represents the global distributions of the contribution of the MUST and the LSt into the  
638 total O<sub>3</sub> columns (Fig.9a; in %), of the adjusted trends for the total O<sub>3</sub> (Fig. 9b in DU/yr) and of  
639 the estimated year for a  $|1.5|$  DU/yr trend detection with a probability of 90% (Fig. 9c). While no  
640 significant change or slightly positive trends in total O<sub>3</sub> after the inflection point in 1997 have  
641 been reported on an annual basis (e.g; Weber et al., 2018), Fig. 9b shows clear significant  
642 changes: negative trend at northern mid- and high latitudes (up to  $\sim 2.0$  DU/yr north of 30°N) and  
643 positive trend over the southern polar region (up to  $\sim 3.0$  DU/yr south of 45°S). Although  
644 counteracting trends between lower and upper stratospheric O<sub>3</sub> have been pointed out in the  
645 recent study of Ball et al. (2018) to explain the non-significant recovery in total O<sub>3</sub>, we find from  
646 IASI a dominance of the LSt decline that translates to negative trends over some regions of the  
647 N.H. mid- and high latitudes in TOC (Fig. 9b). This is explained by the contributions of 45-55%  
648 from the LSt to the total column, *vs*  $\sim 30$ -40% from the MUST (Fig. 9a) in the mid- and polar  
649 regions over the whole year. In addition, the increase in total O<sub>3</sub> at high southern latitudes is  
650 dominated by the LSt, although both layers positively contribute around Antarctica, comparing  
651 to the trend distributions in Fig. 8. Note that most previous ozone trends studies, including Ball  
652 et al. (2018), excluded the polar regions due to limited latitude coverage of some instruments  
653 merged in the data composites.

654

655 While the annual MLR shows a significant dominance of LSt trends over MUST trends in the  
656 northern mid-latitudes and significant constructive trends in the southern latitudes, total O<sub>3</sub>  
657 trends are not ascribed with complete confidence according to the formalism of Tiao et al. (1990)  
658 and Weatherhead et al. (1998) discussed in Section 4.1. The detectability of a specified trend of  
659  $|1.5|$  DU/yr (Fig. 9c), which corresponds to the medium trend derived from MLR in mid-high  
660 latitudes of both hemispheres (Fig. 9b), would need several years of additional measurements to  
661 be unequivocal from IASI on an annual basis (from  $\sim 2022$ – $2024$  over the mid-latitudes and  
662 from  $\sim 2035$  over the polar regions). A higher trend amplitude of  $\sim |2.5|$  DU/yr derived from the  
663 MLR would be observable from  $\sim 2020$ - $2025$  (figure not shown).

664

665 The use of the annual MLR could translate to large systematic uncertainties on trends (implying  
666 large  $\sigma_\epsilon$ ), which induces a longer measurement period required to yield significant trends. These

667 uncertainties could be reduced on a seasonal basis, by attributing different weights to the  
668 seasons, which would help in the categorical detection of a specified trend. This is investigated  
669 in the subsection below by focusing on the winter and the spring periods.

670

### 671 **4.3 Trends in spring and winter**

672

673 The reports on early signs of total O<sub>3</sub> recovery (Salby et al., 2011; Kuttippurath et al., 2013;  
674 Shepherd et al., 2014; Solomon et al., 2016; Kuttippurath and Nair, 2017; Weber et al., 2018)  
675 have all focused on the Antarctic region during spring/summer, when the ozone hole area is at its  
676 maximum extent, i.e. the LSt O<sub>3</sub> levels at minimum values. Kuttippurath et al. (2018) have, in  
677 particular, reported a significant reduction in Antarctic O<sub>3</sub> loss saturation occurrences during  
678 spring. Here we investigate the respective contributions of the LSt and the MUST to the TOC  
679 recovery over the Southern latitudes during spring and also during winter when the minima in O<sub>3</sub>  
680 levels occur in the MUST (down to ~60 DU in polar regions), in comparison with the Northern  
681 latitudes. Figures 10 and 11, respectively, show the S.H. and the N.H. distributions of the  
682 estimated trends from seasonal MLR (left panels) and of the corresponding year required for a  
683 significant detection of |3.0| DU increase per year (right panels) during their respective winter  
684 (JJA and DJF; Fig. 10a and 11a) and spring (SON and MAM; Fig. 10b and 11b) for the total,  
685 MUST and LSt O<sub>3</sub> (top, middle and bottom panels, respectively). Fig. 10 a and b clearly show  
686 significant positive trends over Antarctica and the southernmost latitudes of the Atlantic and  
687 Indian oceans, with amplitudes ranging between ~1-5 DU/yr over latitudes south of ~35-40°S  
688 in total, MUST and LSt O<sub>3</sub> (~3.6±2.7 DU/yr, ~3.0±1.3 DU/yr, ~3.6±3.1 DU/yr and ~3.7±1.7 DU/yr,  
689 ~1.3±0.7 DU/yr, ~3.7±1.6 DU/yr, on spatial averages, respectively over JJA and SON, for the  
690 three O<sub>3</sub> columns). These trends over 10 years are much larger than the amplitude of the  
691 discontinuity in the MUST time series (section 2.1) and than the trends estimated in Sections 4.1  
692 (see Fig.8 for the MUST and the LSt) and 4.2 (see Fig.9 for TOC) over the whole year. In MUST,  
693 significant positive trends are observed during each season over the mid- and polar latitudes of  
694 both hemispheres (Fig. 10 and 11 for the winter and spring periods; the other seasons are not  
695 shown here) but more particularly in winter and in spring where the increase reaches a maximum  
696 of ~4 DU/yr. In the LSt, the distributions are more complex: the trends are significantly negative  
697 in the mid-latitudes of both hemispheres, especially in winter and in spring of the N.H., while in  
698 spring of the S.H., some mid-latitude regions also show near-zero or even positive trends. The  
699 southern polar region shows high significant positive trends in winter/spring (see Fig.10). For the  
700 total O<sub>3</sub> at mid-high latitudes, given the mostly counteracting trends detected in the LSt and in  
701 the MUST and the dominance of the LSt over the MUST (~45-55% from the LSt vs ~30-40%  
702 from the MUST into total O<sub>3</sub> over the whole year;), these latitudes are governed by negative  
703 trends, especially in spring of the N.H. High significant increases are detected over polar regions  
704 in winter/spring of both hemispheres but more particularly in the S.H. where the LSt and MUST  
705 trends are both of positive sign.

706

707 The substantial winter/spring positive trends observed in MUST, LSt and total O<sub>3</sub> levels at high  
708 latitudes of the S.H. (and of the N.H. for the MUST) are furthermore demonstrated to be  
709 detectable from the available IASI measurement period (see Fig. 10, right panels: an assumed  
710 increase of |3.0| DU/yr is detectable from 2016 ± 6 months and from 2018 ± 1 year in the MUST  
711 and the LSt, respectively). The positive trend of ~4 DU/yr measured in polar total O<sub>3</sub> in  
712 winter/spring would be observable from ~2018-2020 ± 1-2 year and the decline of ~-3 DU/yr in  
713 winter/spring of the N.H. in LSt would be detectable from ~2018-2020 ± 9 months (not shown  
714 here). Note that the higher negative trends found above the Pacific at highest latitudes (see Fig.  
715 10) correspond to the regions with longest required measurement period for significant trend  
716 detection and, hence, point to poor regression residuals. About ~50% and ~35% of the  
717 springtime MUST and LSt O<sub>3</sub> variations, respectively, are due to anthropogenic factors (estimated  
718 by VPSC×EESC proxy and linear trend in MLR models). This suggests that O<sub>3</sub> changes  
719 especially in the LSt are mainly governed by dynamics, which contributes to a later projected  
720 trend-detection year in comparison with the MUST (Fig. 10 and 11) and which may hinder the O<sub>3</sub>  
721 recovery process.

722

723 Overall, the large positive trends estimated concurrently in LSt, MUST and total O<sub>3</sub> over the  
724 Antarctic region in winter/spring likely reflect the healing of the ozone layer with a decrease of  
725 polar ozone depletion (Solomon et al., 2016) and, hence, demonstrate the efficiency of the  
726 Montreal protocol. To the best of our knowledge, these results represent the first detection of a  
727 significant recovery in the stratospheric and the total O<sub>3</sub> columns over the Antarctic from one  
728 single satellite dataset.

729

#### 730 **4.4 Speeding up in O<sub>3</sub> changes**

731

732 Positive trends in total O<sub>3</sub> have already been determined earlier by Solomon et al. (2016) and by  
733 Weber et al. (2018) over Antarctica during September over earlier periods (~2.5±1.5DU/yr over  
734 2000-2014 and 8.2±6.2%/dec over 2000-2016, respectively). The larger trends derived from the  
735 IASI records (see Fig.10b; ~3.7±1.7 DU/yr or ~14.4±5.8%/dec on average in TOC during SON)  
736 suggest that the O<sub>3</sub> response could be speeding up due to the accelerating decline of O<sub>3</sub> depleting  
737 substances (ODS) resulting from the Montreal Protocol. This has been investigated here by  
738 estimating the change in trend in MUST, LSt and total O<sub>3</sub> over the IASI mission. Knowing that  
739 the length of the measurement period is an important criterion for reducing systematic errors in  
740 the trend coefficient determination (i.e. the specific length of natural mode cycles should be  
741 covered to avoid any possible compensation effect between the covariates), the ozone response  
742 to each natural driver (including VPSC) taken from their adjustment over the whole IASI period  
743 (2008-2017; Section 3, Fig.5) is kept fixed. The linear trend term only is adjusted over variable  
744 measurement periods that all end in December 2017, by using a single linear iteratively  
745 reweighted least squares regression applied on gridded daily IASI time series, after all the  
746 sources of natural variability fitted over the full IASI period are removed (typical examples of

747 linear trend adjustment can be found in Fig. S2 of the supplementary materials). The  
748 discontinuity found in the MUST IASI O<sub>3</sub> records on September 2010 (see Section 2.1) is not  
749 taken into account in the regression; hence, it might over-represent the trends estimated over  
750 periods that start before the jump (i.e. 2008-2017, 2009-2017, 2010-2017). The zonally averaged  
751 results are displayed in Fig. 12 for the statistically significant total, MUST and LSt O<sub>3</sub> trends and  
752 their associated uncertainty (accounting for the autocorrelation in the noise residuals; in the 95%  
753 confidence level) estimated from an annual regression. Note that the results are only shown for  
754 periods starting before 2015 as too short periods induce too large standard errors. In the LSt, a  
755 clear speeding up in the southern polar O<sub>3</sub> recovery is observed with amplitude ranging from  
756  $\sim 1.5 \pm 0.4$  DU/yr over 2008-2017 to  $\sim 5.5 \pm 2.5$  DU/yr over 2015-2017 on zonal averages.  
757 Similarly, a speeding of the O<sub>3</sub> decline at northern mid-latitudes is found with values ranging  
758 between  $\sim -0.7 \pm 0.2$  DU/yr over 2008-2017 and  $\sim -2.8 \pm 1.2$  DU/yr over 2015-2017. In the MUST, a  
759 weaker increase is observed over the year around  $\sim 60^\circ$  latitude of the S.H. (from  $\sim 0.8 \pm 0.2$  DU/yr  
760 over 2008-2017 to  $\sim 2.5 \pm 1.3$  DU/yr over 2015-2017). Given the positive acceleration in both LSt  
761 and MUST O<sub>3</sub> in the S.H., this is where the total O<sub>3</sub> record is characterized by the largest  
762 significant recovery (from  $\sim 1.7 \pm 0.7$  DU/yr over 2008-2017 to  $\sim 8.0 \pm 3.5$  DU/yr over 2015-2017).  
763 Surprisingly, the speeding up in the O<sub>3</sub> decline in the N.H. is more pronounced in the total O<sub>3</sub>  
764 (from  $\sim -1.0 \pm 0.4$  DU/yr over 2008-2017 to  $\sim -5.0 \pm 2.5$  DU/yr over 2015-2017) compared to the  
765 LSt, despite the opposite trend in MUST O<sub>3</sub>. This could reflect the O<sub>3</sub> decline observed in the  
766 northern latitudes in the troposphere ( $\sim -0.5$  DU/yr over 2008-2016; cfr Wespes et al., 2018)  
767 which is included in the total column.

768  
769 Overall, the larger annual significant trend amplitudes derived over the last few years of total,  
770 MUST and LSt O<sub>3</sub> measurements, compared with those derived from the whole studied period  
771 (Sections 4.1 and 4.2) and from earlier studies, translate to trends that remain detectable over the  
772 increasing uncertainty associated with the shorter and shorter time segments (see Fig. S3 of the  
773 supplementary materials), especially in both LSt and total O<sub>3</sub> in the S.H. This demonstrates that  
774 we progress towards a significant emergence and speeding up of O<sub>3</sub> recovery process in the  
775 stratosphere over the whole year. Nevertheless, we calculated that additional years of IASI  
776 measurements would help in confirming the changes in O<sub>3</sub> recovery and decline over the IASI  
777 period (e.g.  $\sim 4$  additional years are required to verify the trends calculated over the 2015-2017  
778 segment in the highest latitudes in LSt). In addition, a longer measurement period would be  
779 useful to derive trends over successive segments of same length that are long enough to reduce  
780 the uncertainty, in order to make the trend and its associated uncertainty more comparable across  
781 the fit.

782

## 783 **5 Summary and conclusion**

784

785 In this study, we have analysed the changes in stratospheric O<sub>3</sub> levels sounded by IASI-A by  
786 examining the global pictures of natural and anthropogenic sources of O<sub>3</sub> changes independently



787 in the lower (150-25 hPa) and in the mid-upper stratosphere (<25 hPa). We have exploited to that  
788 end a multi-linear regression model that has been specifically developed for the analysis of  
789 stratospheric processes by including a series of drivers known to have a causal relationship to  
790 natural stratospheric O<sub>3</sub> variations, namely SF, QBO-10, QBO-30, NAO, AAO, ENSO, AERO,  
791 EPF and VPSC. We have first verified the representativeness of the O<sub>3</sub> response to each of these  
792 natural drivers and found for most of them characteristic patterns that are in line with the current  
793 knowledge of their dynamical influence on O<sub>3</sub> variations. One of the most important finding  
794 related to the O<sub>3</sub> driver analysis relied on the detection of a very clear time lag of 3 months in the  
795 O<sub>3</sub> response to ENSO in the LSt, with a pronounced contrast between an in-phase response in the  
796 extra-tropics and an out-of-phase response in the tropics, which is consistent with the ENSO-  
797 modulated dynamic. The 3-month lag observed in the lower stratosphere is also coherent with  
798 the 4- to -6 months lag detected from a previous study in the troposphere (Wespes et al., 2017)  
799 and further supports the stratospheric pathway suggested in Butler et al. (2014) to explain an  
800 ENSO influence over a long distance. The representativeness of the influence of the O<sub>3</sub> drivers  
801 was also confirmed on a seasonal basis (e.g. high ENSO-lag3 effect in spring, strong VPSC and  
802 AERO influences during the austral spring ...). These results have verified the performance of  
803 the regression models (annual and seasonal) to properly discriminate between natural and  
804 anthropogenic drivers of O<sub>3</sub> changes. The anthropogenic influence has been evaluated with the  
805 linear trend adjustment in the MLR. The main results are summarized as follows:

- 806
- 807 (i) A highly probable (within 95%) recovery process is derived from the annual MLR at high  
808 southern latitudes in the two stratospheric layers and, therefore, in the total column. It  
809 is also derived at high northern latitudes in the MUST. However, a longer period of  
810 IASI measurements is needed– to unequivocally demonstrate a positive trend on  
811 annual basis in the IASI record. Only ~2-3 additional years of IASI measurements are  
812 required in the MUST.
  - 813
  - 814 (ii) A likely O<sub>3</sub> decline (within 95%) is measured in the lower stratosphere at mid-latitudes,  
815 specifically, of the N.H., but it would require an additional ~7 years of IASI  
816 measurements to be categorically confirmed. Given the large contribution from the  
817 LSt to the total column (~45-50% from LSt vs ~35% from the MUST into TOCs), the  
818 decline is also calculated in total O<sub>3</sub> with ~4-6 years of additional measurements for  
819 the trend to be unequivocal.
  - 820
  - 821 (iii) A significant O<sub>3</sub> recovery is categorically found in the two stratospheric layers  
822 (>~35°N/S in the MUST and >~45°S in the LSt) as well as in the total column  
823 (>~45°S) during the winter/spring period, which confirms previous studies that  
824 showed healing in the Antarctic O<sub>3</sub> hole with a decrease of its areal extent. These  
825 results verify the efficacy of the ban on O<sub>3</sub> depleting substances imposed by the

826 Montreal protocol and its amendments, throughout the stratosphere and in the total  
827 column, from only one single satellite dataset for the first time.

828  
829 (iv) The decline observed in LSt O<sub>3</sub> at northern mid-latitudes is unequivocal over the  
830 available IASI measurements in winter/spring of the N.H. The exact reasons for that  
831 decline are still unknown but O<sub>3</sub> changes in the LSt are estimated to be mainly  
832 attributable to dynamics which likely perturbs the healing of LSt and total O<sub>3</sub> in the  
833 N.H.

834  
835 (v) A significant speeding up (within 95%) in that decline is measured in LSt and total O<sub>3</sub>  
836 over the last 10 years (from  $\sim -0.7 \pm 0.2$  DU/yr over 2008-2017 to  $\sim -2.8 \pm 1.2$  DU/yr  
837 over 2015-2017 in LSt O<sub>3</sub> on zonal averages). Even if the acceleration cannot be  
838 categorically confirmed yet, it is of particular urgency to understand its causes for  
839 apprehending its possible impact on the O<sub>3</sub> layer and on future climate changes.

840  
841 (vi) A clear and significant speeding up (within 95%) in stratospheric and total O<sub>3</sub> recovery  
842 is measured at southern latitudes (e.g. from  $\sim 1.5 \pm 0.4$  DU/yr over 2008-2017 to  
843  $\sim 5.5 \pm 2.5$  DU/yr over 2015-2017 in the LSt), which translate to trend values that  
844 would be categorically detectable in the next few years on an annual basis. It  
845 demonstrates that we are currently progressing towards a substantial emergence in O<sub>3</sub>  
846 healing in the stratosphere over the whole year in the S.H.

847  
848 Additional years of IASI measurements that will be provided by the operational IASI-C (2018)  
849 on flight and the upcoming IASI-Next Generation (IASI-NG) instrument onboard the Metop  
850 Second Generation (Metop-SG) series of satellites would be of particular interest to confirm and  
851 monitor, in the near future and over a longer period, the speeding up in the O<sub>3</sub> healing of the S.H.  
852 as well as in the LSt O<sub>3</sub> decline measured at mid-latitudes of the N.H. IASI-NG/Metop-SG is  
853 expected to extend the data record much further in the future (Clerbaux and Crevoisier, 2013;  
854 Crevoisier et al., 2014).

855

#### 856 **Data availability**

857  
858 The IASI O<sub>3</sub> data processed with FORLI-O<sub>3</sub> v0151001 can be downloaded from the Aeris portal  
859 at: <http://iasi.aeris-data.fr/O3/> (last access: 13 September 2019).

860

#### 861 **Author contribution**

862  
863 C.W. performed the analysis, wrote the manuscript and prepared the figures. D.H. was  
864 responsible for the retrieval algorithm development and the processing of the IASI O<sub>3</sub> dataset.  
865 All co-authors contributed to the analysis and reviewed the manuscript.

866  
867  
868  
869  
870  
871  
872  
873  
874  
875  
876  
877  
878  
879  
880  
881  
882  
883  
884  
885  
886  
887  
888  
889  
890  
891  
892  
893  
894  
895  
896  
897  
898  
899  
900  
901  
902  
903  
904  
905

**Competing interests**

The authors declare that they have no conflict of interest.

**Acknowledgments**

IASI has been developed and built under the responsibility of the Centre National d'Etudes Spatiales (CNES, France). It is flown onboard the Metop satellites as part of the EUMETSAT Polar System. The IASI L1 data are received through the EUMETCast near real time data distribution service. We acknowledge the financial support from the ESA O<sub>3</sub>-CCI and Copernicus O<sub>3</sub>-C3S projects. FORLI-O<sub>3</sub> is being implemented at Eumetsat with the support of the AC SAF project. The research in Belgium is also funded by the Belgian State Federal Office for Scientific, Technical and Cultural Affairs and the European Space Agency (ESA Prodex IASI Flow and B-AC SAF). We acknowledge Ingo Wohltmann (Alfred Wagner Institute, Postdam, Germany) as well as Beiping Luo (Institute for Atmosphere and Climate, ETH Zurich, Switzerland) and Larry Thomason (NASA Langley Research Center, Hampton, USA), for processing and providing datasets of volume of polar stratospheric clouds and of sulfuric acid extinction coefficients, respectively. We are also grateful to Maxime Prignon (Université de Liège, Liège, Belgium) for providing several years of BASCOE simulations.

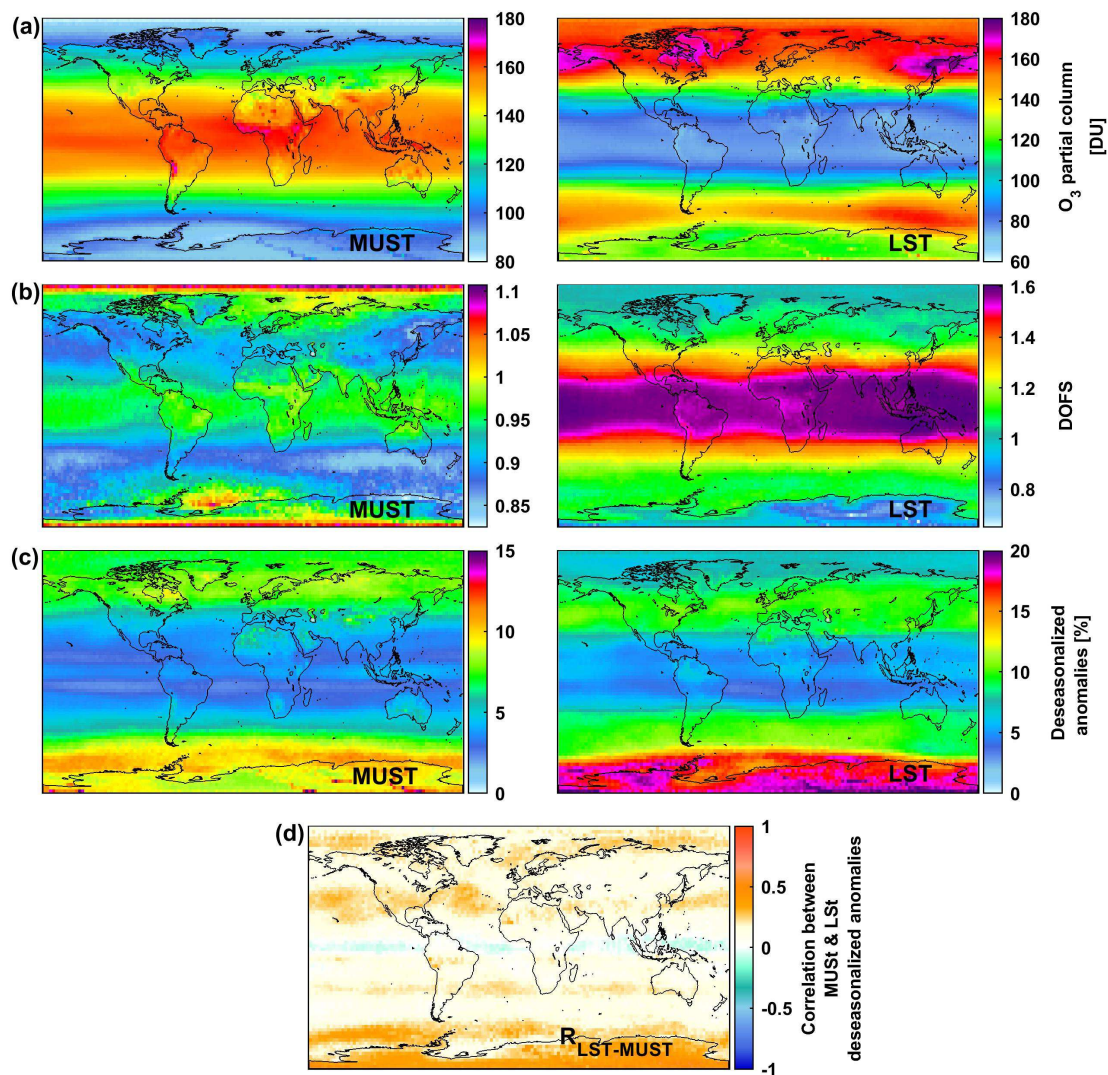
906 **Table 1** List of the explanatory variables used in the multi-linear regression model applied on  
 907 IASI stratospheric O<sub>3</sub>, their temporal resolution and their sources.  
 908

Proxy	Description ( <i>resolution</i> )	Sources
<b>F10.7</b>	The 10.7 cm solar radio flux ( <i>daily</i> )	NOAA National Weather Service Climate Prediction Center: <a href="ftp://ftp.ngdc.noaa.gov/STP/space-weather/solar-data/solar-features/solar-radio/noontime-flux/penticton/penticton_adjusted/listings/listing_drao_noontime-flux-adjusted_daily.txt">ftp://ftp.ngdc.noaa.gov/STP/space-weather/solar-data/solar-features/solar-radio/noontime-flux/penticton/penticton_adjusted/listings/listing_drao_noontime-flux-adjusted_daily.txt</a>
<b>QBO<sup>10</sup></b> <b>QBO<sup>30</sup></b>	Quasi-Biennial Oscillation index at 10hPa and 30hPa ( <i>monthly</i> )	Free University of Berlin: <a href="http://www.geo.fu-berlin.de/en/met/ag/strat/produkte/qbo/">www.geo.fu-berlin.de/en/met/ag/strat/produkte/qbo/</a>
<b>EPF</b>	Vertical component of Eliassen-Palm flux crossing 100 hPa, averaged over 45°-75° for each hemisphere and accumulated over the 3 or 12 last months depending on the time period and the latitude (see text for more details) ( <i>daily</i> )	Calculated at ULB from the NCEP/NCAR gridded reanalysis: <a href="https://www.esrl.noaa.gov/psd/data/gridded/data.ncep.reanalysis.html">https://www.esrl.noaa.gov/psd/data/gridded/data.ncep.reanalysis.html</a>
<b>AERO</b>	Stratospheric volcanic aerosols; Vertically integrated sulfuric acid extinction coefficient at 12 μm over 150-25 hPa and 25-2hPa, averaged over the tropics and the extra-tropics north and south (see text for more details) ( <i>monthly</i> )	Extinction coefficients processed at the Institute for Atmosphere and Climate (ETH Zurich, Switzerland; Thomason et al., 2018)
<b>VPSC</b>	Volume of Polar Stratospheric Clouds for the N.H. and the S.H. multiplied by the equivalent effective stratospheric chlorine (EESC) and accumulated over the 3 or 12 last months (see text for details) ( <i>daily</i> )	Processed at the Alfred Wagner Institute (AWI, Postdam, Germany; Ingo Wolthmann, private communication)  EESC taken from the Goddard Space Flight Center: <a href="https://acd-ext.gsfc.nasa.gov/Data_services/automailer/index.html">https://acd-ext.gsfc.nasa.gov/Data_services/automailer/index.html</a>
<b>ENSO</b>	Multivariate El Niño Southern Oscillation Index (MEI) (2- <i>monthly averages</i> )	NOAA National Weather Service Climate Prediction Center: <a href="http://www.esrl.noaa.gov/psd/enso/mei/table.html">http://www.esrl.noaa.gov/psd/enso/mei/table.html</a>
<b>NAO</b>	North Atlantic Oscillation index for the N.H. ( <i>daily</i> )	<a href="ftp://ftp.cpc.ncep.noaa.gov/cwlinks/norm.daily.nao.index.b500101.curent.ascii">ftp://ftp.cpc.ncep.noaa.gov/cwlinks/norm.daily.nao.index.b500101.curent.ascii</a>
<b>AAO</b>	Antarctic Oscillation index for the S.H. ( <i>daily</i> )	<a href="ftp://ftp.cpc.ncep.noaa.gov/cwlinks/norm.daily.aao.index.b790101.curent.ascii">ftp://ftp.cpc.ncep.noaa.gov/cwlinks/norm.daily.aao.index.b790101.curent.ascii</a>
<b>GEO</b>	Geopotential height at 200 hPa (2.5°x2.5° gridded) ( <i>daily</i> )	<a href="http://apps.ecmwf.int/datasets/data/interim-full-daily/?levtype=pl">http://apps.ecmwf.int/datasets/data/interim-full-daily/?levtype=pl</a>
<b>PV</b>	Potential vorticity at 200 hPa (2.5°x2.5° gridded) ( <i>daily</i> )	

909 **Figure captions**

910

911



912

913 **Fig.1.** Global distribution of (a) daily O<sub>3</sub> columns (in Dobson Units - DU), (b) associated DOFS,

914 (c) absolute deseasonalized anomalies (in %) averaged over January 2008 – December 2017 in

915 the MUST (Mid-Upper Stratosphere: >25 hPa; left panels) and in the LSt (Lower Stratosphere:

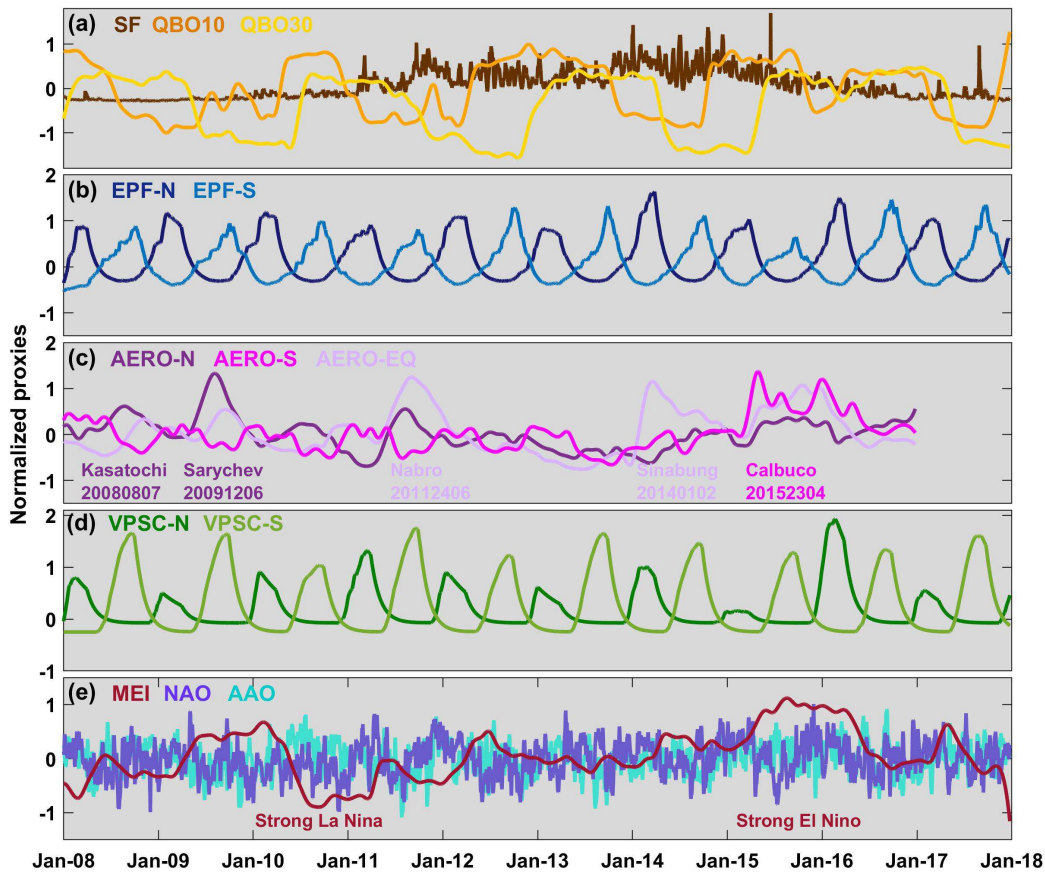
916 150-25hPa; right panels). (d) shows the correlation coefficients between the daily O<sub>3</sub>

917 deseasonalized anomalies in the MUST and in the LSt. Note that the scales are different between

918 MUST and LSt.

919

920

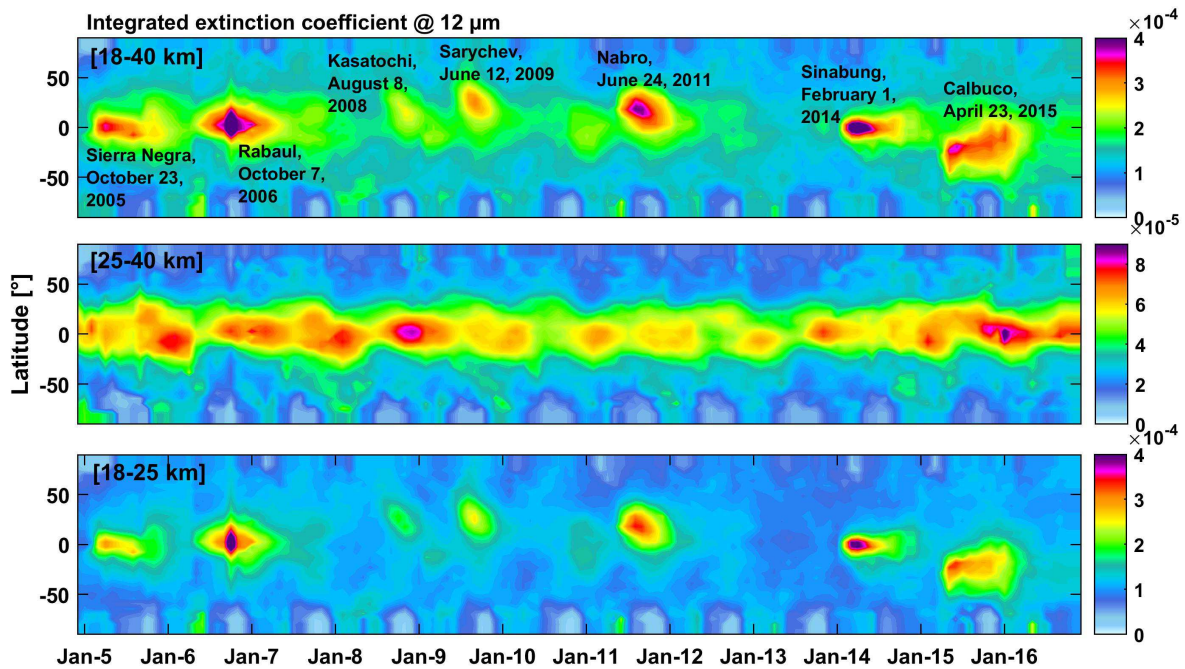


921  
922

923 **Fig.2.** Normalized proxies as a function of time for the period covering January 2008 to  
 924 December 2017 for (a) the F10.7 cm solar radio flux (SF) and the equatorial winds at 10  
 925 (QBO10) and 30 hPa (QBO30), respectively, (b) the upward components of the EP flux crossing  
 926 100 hPa accumulated over time and averaged over the 45°-75° latitude band for each  
 927 hemispheres (EPF-N and EPF-S), (c) the extinction coefficients at 12 μm vertically integrated  
 928 over the stratospheric O<sub>3</sub> column (from 150-2hPa) and averaged over the extra-tropics north and  
 929 south (22.5°-90°N/S; AERO-N and AERO-S) and over the tropics (22.5°S-22.5°N; AERO-EQ)  
 930 (the main volcanic eruptions are indicated), (d) the volume of polar stratospheric clouds  
 931 multiplied by the equivalent effective stratospheric chlorine (EESC) and accumulated over time  
 932 for the north and south hemispheres (VPSC-N and VPSC-S) and (e) the El Niño Southern  
 933 (ENSO), North Atlantic (NAO) and Antarctic (AAO) oscillations.

934  
935

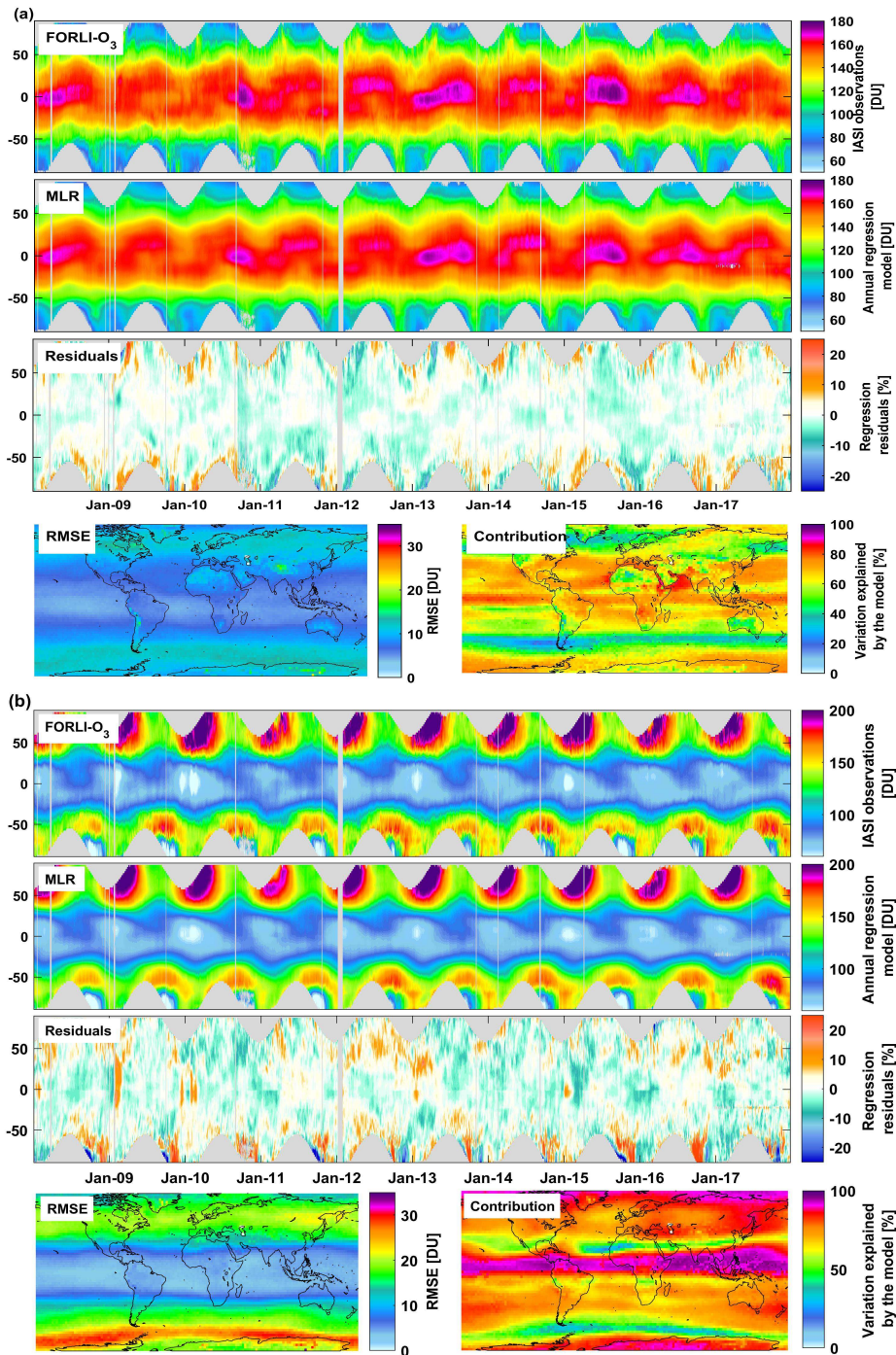




936  
937

938 **Fig.3:** Latitudinal distribution of volcanic sulfuric acid extinction coefficient at 12  $\mu\text{m}$  integrated  
 939 over the stratosphere (top panel), over the middle stratosphere (middle panel) and the lower  
 940 stratosphere (bottom panel) as a function of time from 2005 to 2017. The dataset consists of  
 941 monthly mean aerosol data merged from SAGE, SAM, CALIPSO, OSIRIS, 2D-model-  
 942 simulation and Photometer (processed at NASA Langley Research Center, USA and ETH  
 943 Zurich, Switzerland).

944  
945  
946  
947  
948  
949  
950  
951  
952  
953  
954  
955  
956  
957  
958  
959  
960



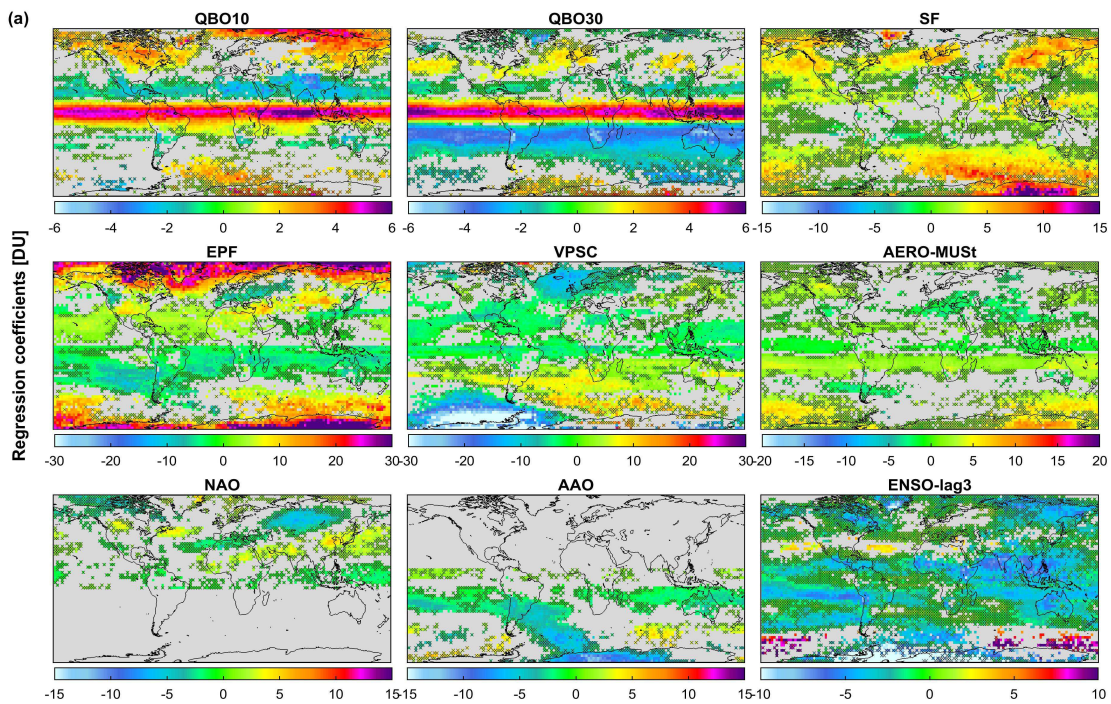
961

962  
963

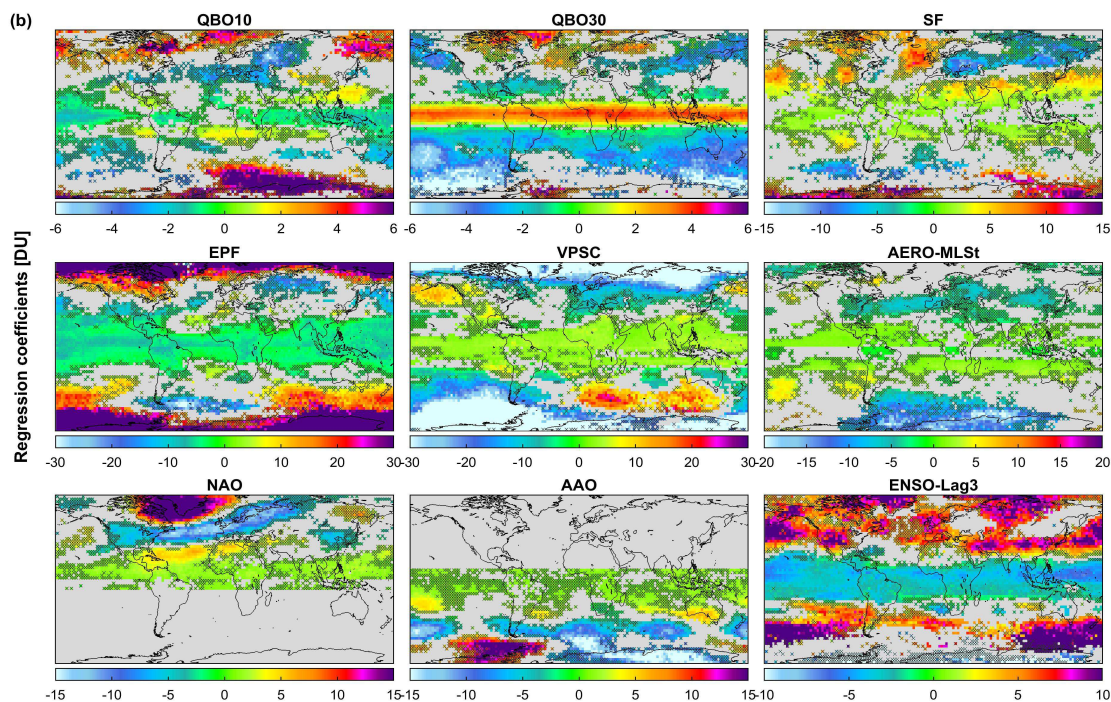
964 **Fig.4:** Latitudinal distribution of (a) MUST O<sub>3</sub> column and (b) LSt O<sub>3</sub> columns as a function of  
 965 time observed from IASI (in DU; top panels), simulated by the annual regression model (in DU,  
 966 second panels) and of the regression residuals (in %; third panels). Global distribution of *RMSE*  
 967 of the regression residual (in DU) and fraction of the variation in IASI data explained by the  
 968 regression model calculated as  $[100 \times (\sigma(O_3^{Fitted\_model}(t)) / \sigma(O_3(t)))]$  (in %; fourth panels).



969

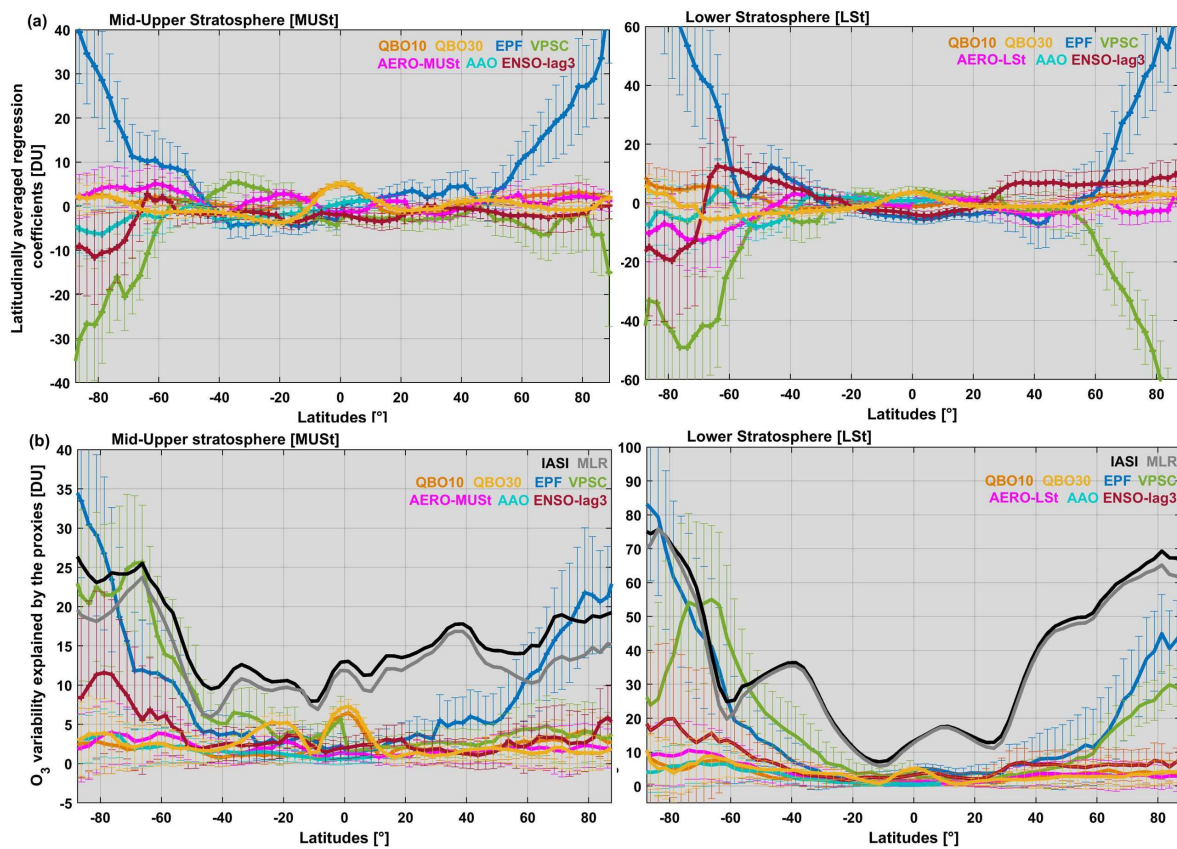


970



971

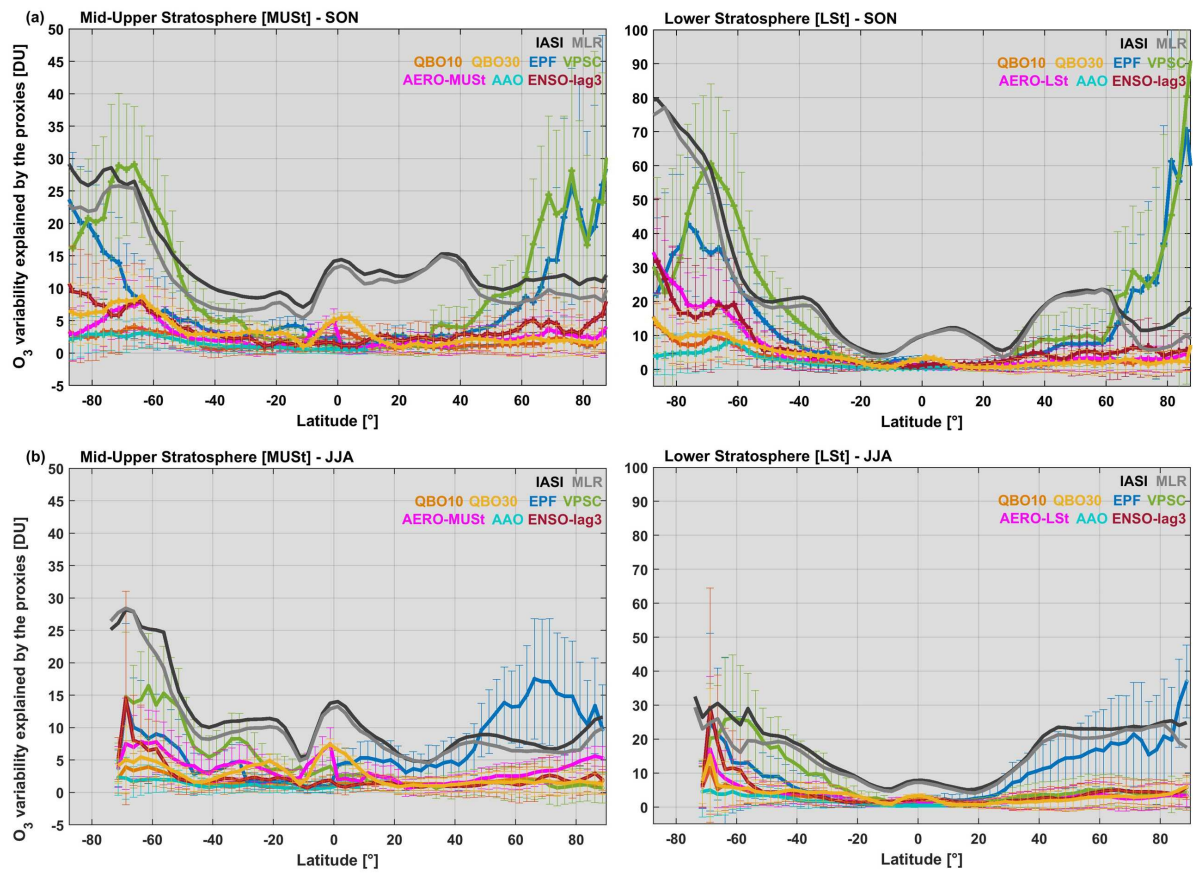
972 **Fig.5:** Global distribution of the annual regression coefficient estimates (in DU) for the main O<sub>3</sub>  
 973 drivers in (a) MUST and in (b) LSt: QBO10, QBO30, SF, EPF, VPSC, AERO, NAO, AAO and  
 974 ENSO (ENSO-lag3 for both LSt and MUST). Grey areas and crosses refer to non-significant grid  
 975 cells in the 95% confidence limit. Note that the scales differ among the drivers.



976  
 977  
 978  
 979  
 980  
 981  
 982  
 983  
 984  
 985  
 986  
 987  
 988

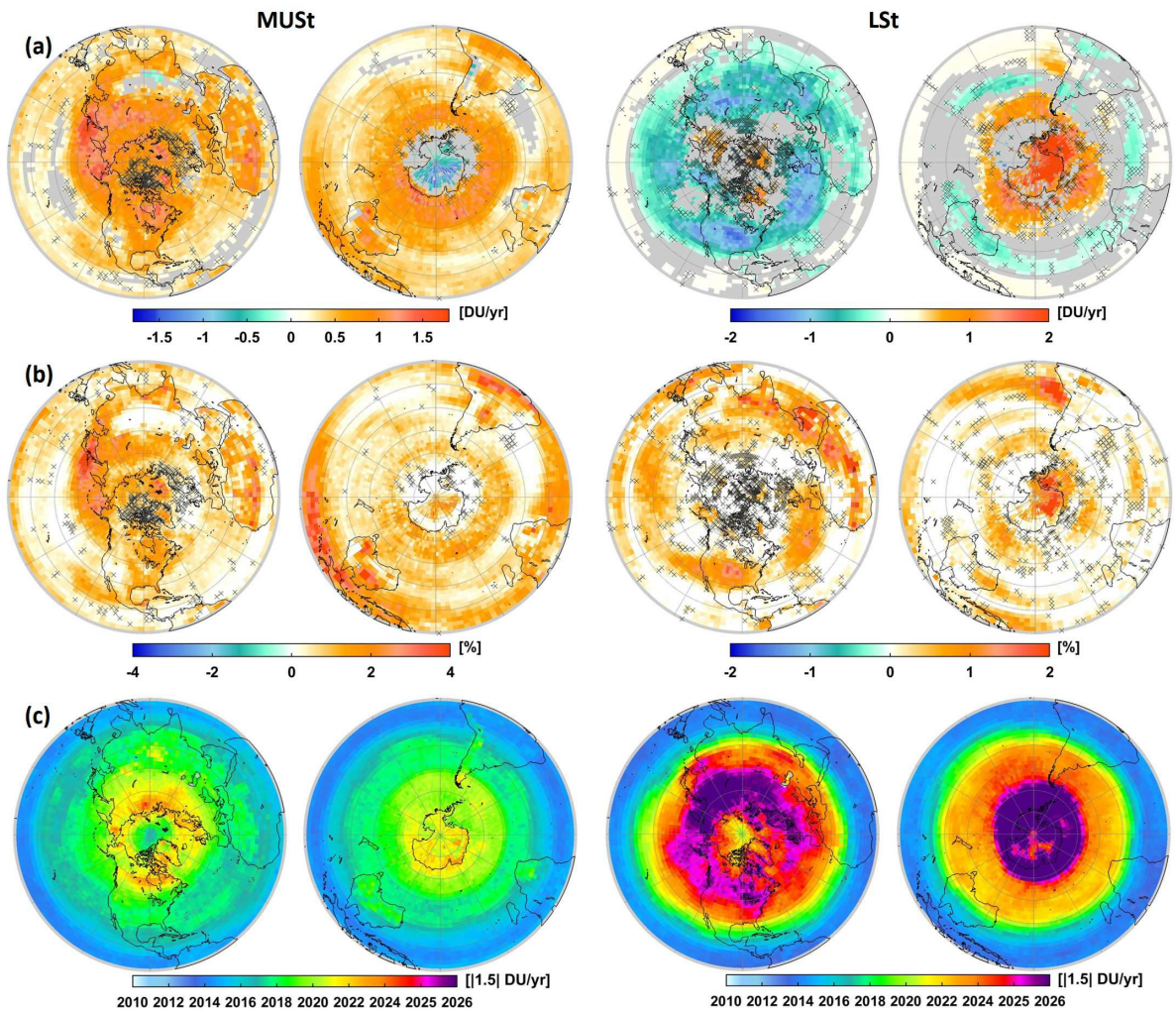
**Fig.6:** Latitudinal distributions (a) of fitting regression coefficients for various O<sub>3</sub> drivers (QBO10, QBO30, EPF, VPSC, AERO, AAO and ENSO-lag3; in DU) and (b) of 2 $\sigma$  O<sub>3</sub> variability due to variations in those drivers (in DU) from the annual MLR in MUST and LSt (left and right panels respectively). Vertical bars correspond (a) to the uncertainty of fitting coefficients at the 2 $\sigma$  level and (b) to the corresponding error contribution into O<sub>3</sub> variation. Note that the scales are different.





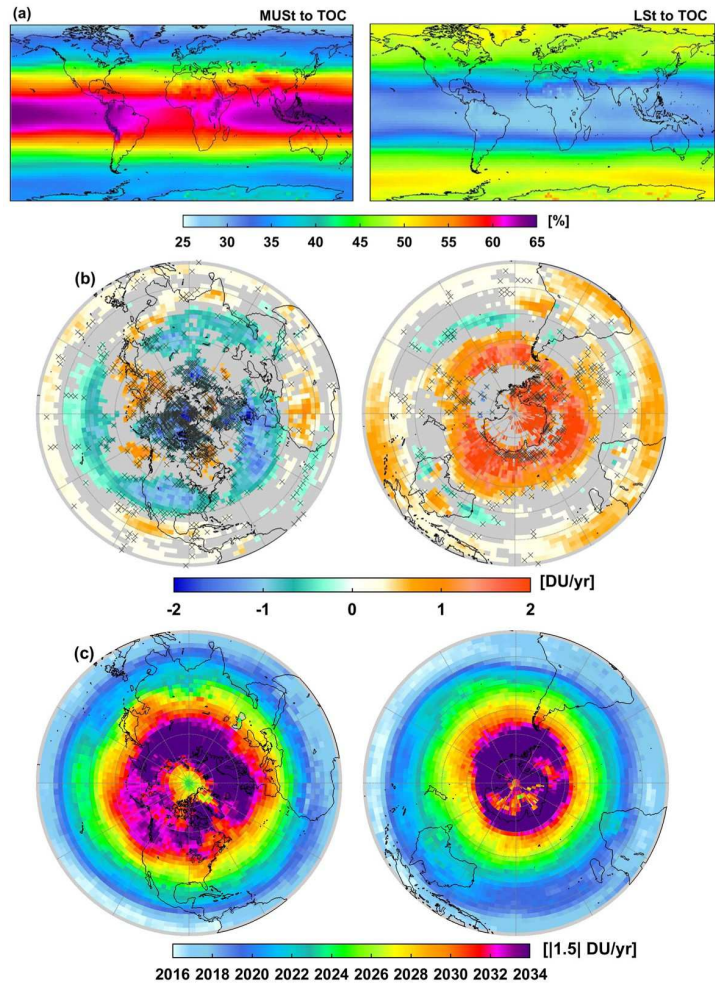
989  
 990  
 991  
 992  
 993  
 994

**Fig.7:** Same as Fig. 6b but for (a) the austral winter and (b) the austral spring periods (JJA and SON, respectively) from the seasonal MLR. Note that the scales are different.



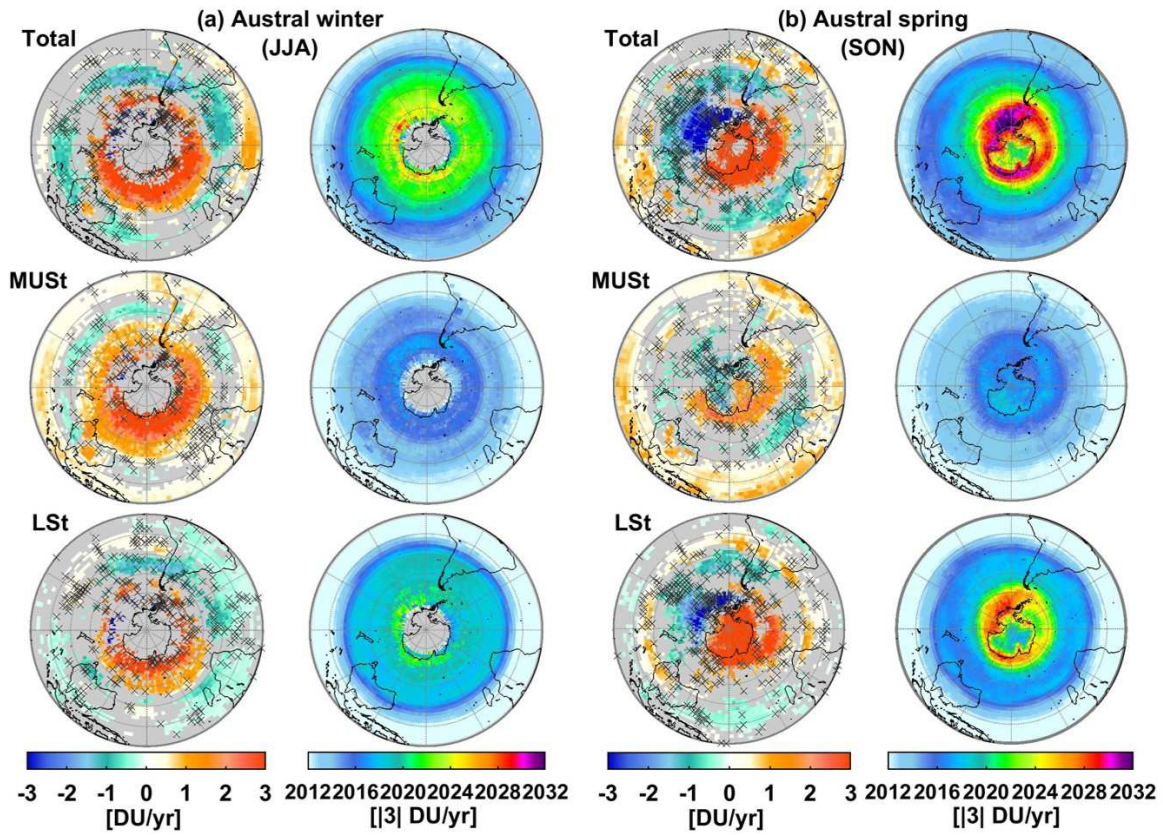
995  
 996  
 997  
 998  
 999  
 1000  
 1001  
 1002  
 1003  
 1004

**Fig. 8:** Global distribution (a) of the estimated annual trends (in DU/yr; grey areas and crosses refer to non-significant grid cells in the 95% confidence limit), (b) of the IASI sensitivity to trend calculated as the differences between the *RMSE* of the annual MLR fits with and without linear trend term  $[(RMSE_{w/o\_LT} - RMSE_{with\_LT})/RMSE_{with\_LT} \times 100]$  (in %), (c) of the estimated year for a significant detection (with a probability of 90%) of a given trend of  $|1.5|$  DU/yr starting in January 2008 in MUST and LSt O<sub>3</sub> columns (left and right panels, respectively). Note that the scales are different for the two layers.



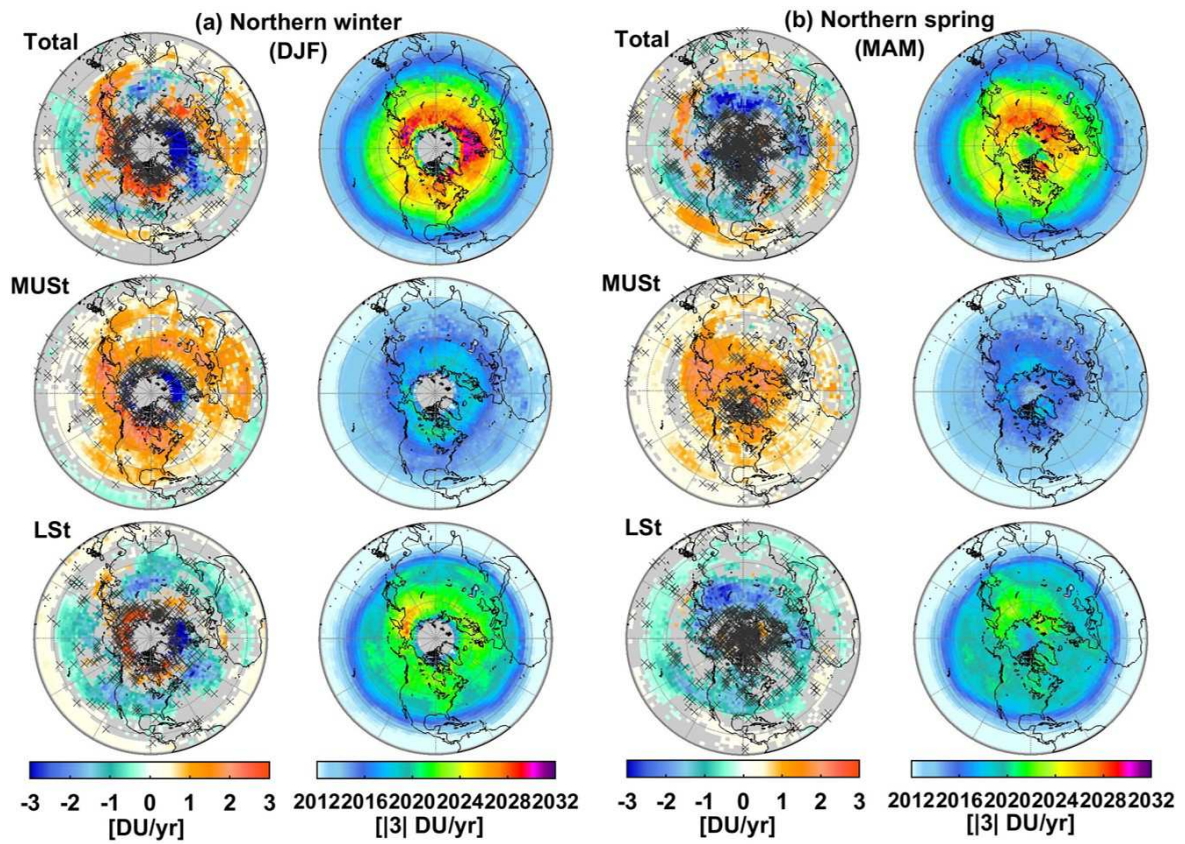
1005  
 1006 **Fig.9:** Global distribution of (a) the contribution (in %) of MUST and LSt into the total O<sub>3</sub> (left  
 1007 and right panels respectively) averaged over January 2008 – December 2017, (b) fitted trends in  
 1008 total O<sub>3</sub> (in DU/yr; the grey areas and crosses refer to the non-significant grid cells in the 95%  
 1009 confidence limit) and (c) estimated year for the detection of a significant trend in total O<sub>3</sub> (with a  
 1010 probability of 90%) for a given trend of |1.5| DU/yr starting on January 2008.  
 1011





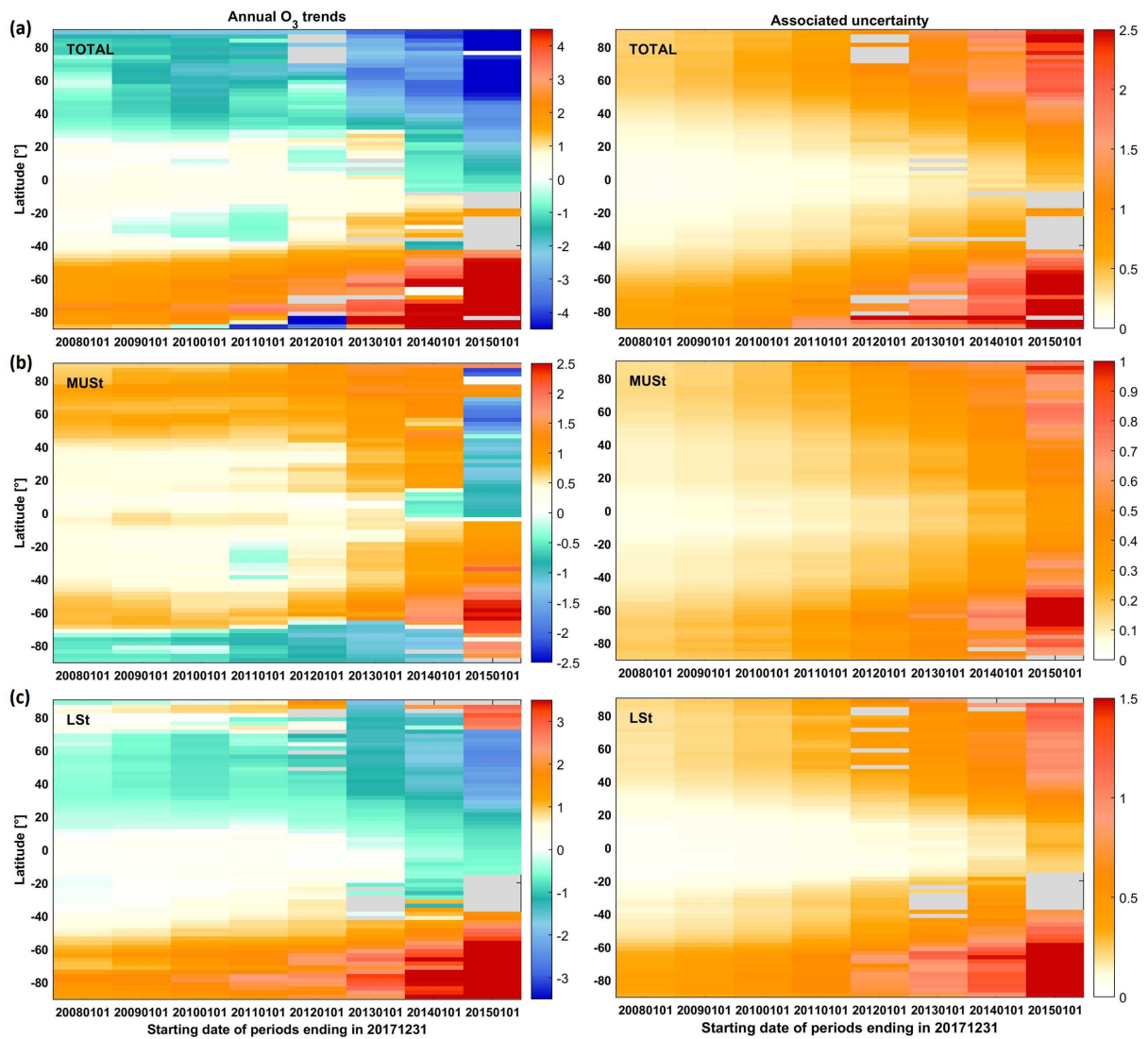
1012  
 1013  
 1014  
 1015  
 1016  
 1017  
 1018  
 1019  
 1020  
 1021  
 1022  
 1023  
 1024  
 1025  
 1026  
 1027  
 1028  
 1029  
 1030

**Fig.10:** Hemispheric distribution (a) in austral winter (JJA) and (b) in austral spring (SON) of the estimated trends in total, MUST and LSt O<sub>3</sub> columns (left panels: top, middle and bottom, respectively; in DU/yr; the grey areas and crosses refer to the non-significant grid cells in the 95% confidence limits) and of the corresponding estimated year for a significant trend detection (with a probability of 90%) of a given trend of  $|3|$  DU/yr starting at January 2008 (right panels: top, middle and bottom, respectively).



1031  
 1032  
 1033  
 1034  
 1035  
 1036  
 1037

**Fig. 11:** Same as Fig. 10 but (a) for the winter (DJF) and (b) for the spring (MAM) of the northern Hemisphere.



1038  
 1039 **Fig.12:** Evolution of estimated linear trend (DU/yr) and associated uncertainty accounting for the  
 1040 autocorrelation in the noise residuals (DU/yr; in the 95% confidence level) in (a) total, (b) MUSSt  
 1041 and (c) LSt O<sub>3</sub> columns, as a function of the covered IASI measurement period ending in  
 1042 December 2017, with all natural contributions estimated from the whole IASI period (2008-  
 1043 2017). Note that the scales are different between the columns.

1044  
 1045  
 1046  
 1047  
 1048  
 1049  
 1050  
 1051



1052 **References**

1053

1054 Anderson, J., Russell, J. M., Solomon, S., and Deaver, L. E.: Halogen Occultation Experiment  
1055 confirmation of stratospheric chlorine decreases in accordance with the Montreal Protocol, *J.*  
1056 *Geophys. Res.-Atmos.*, 105, 4483–4490, <https://doi.org/10.1029/1999JD901075>, 2000.

1057

1058 Baldwin, M. P., L.J. Gray, T.J. Dunkerton, K. Hamilton, P.H. Haynes, W.J. Randel, J.R. Holton,  
1059 M.J. Alexander, I. Hirota, T. Horinouchi, D.B.A. Jones, J.S. Kinnersley, C. Marquardt, K. Sato,  
1060 and M. Takahashi: The quasi-biennial oscillation, *Rev. Geophys.*, 39, 179–230,  
1061 doi:10.1029/1999RG000073, 2001.

1062

1063 Ball, W. T., Alsing, J., Mortlock, D. J., Staehelin, J., Haigh, J. D., Peter, T., Tummon, F., Stübi,  
1064 R., Stenke, A., Anderson, J., Bourassa, A., Davis, S. M., Degenstein, D., Frith, S., Froidevaux,  
1065 L., Roth, C., Sofieva, V., Wang, R., Wild, J., Yu, P., Ziemke, J. R., and Rozanov, E. V.:  
1066 Evidence for a continuous decline in lower stratospheric ozone offsetting ozone layer recovery,  
1067 *Atmos. Chem. Phys.*, 18, 1379–1394, <https://doi.org/10.5194/acp-18-1379-2018>, 2018.

1068

1069 Barnston, A. G. and Livezey, R. E.: Classification, seasonality and persistence of low-frequency  
1070 atmospheric circulation patterns, *Mon. Weather. Rev.* 115: 1083–1126, 1987.

1071

1072 Boynard, A., D. Hurtmans, K. Garane, F. Goutail, J. Hadji-Lazaro, M. E. Koukouli, C. Wespes,  
1073 C. Vigouroux, A. Keppens, J.-P. Pommereau, A. Pazmino, D. Balis, D. Loyola, P. Valks, R.  
1074 Sussmann, D. Smale, P.-F. Coheur and C. Clerbaux: Validation of the IASI FORLI/Eumetsat O<sub>3</sub>  
1075 products using satellite (GOME-2), ground-based (Brewer-Dobson, SAOZ, FTIR) and  
1076 ozonesonde measurements, *Atmos. Meas. Tech.*, 11, 5125–5152, 2018.

1077

1078 Brasseur, G.: The response of the middle atmosphere to long-term and short-term solar  
1079 variability: A two-dimensional model, *J. Geophys. Res.*, 98, 23 079–23 090, 1993.

1080

1081 Brönnimann, S., Luterbacher, J., Staehelin, J., Svendby, T. M., Hansen, G., and Svenøe, T.:  
1082 Extreme climate of the global troposphere and stratosphere 1940–1942 related to El Nino,  
1083 *Nature*, 431, 971–974, 2004.

1084

1085 Brunner, D., Staehelin, J., Maeder, J. A., Wohltmann, I., and Bodeker, G. E.: Variability and  
1086 trends in total and vertically resolved stratospheric ozone based on the CATO ozone data set,  
1087 *Atmos. Chem. Phys.*, 6, 4985–5008, doi:10.5194/acp-6-4985-2006, 2006.

1088

1089 Buffet, L., Villaret, C., Jacquette, E., Vandermarcq, O., Astruc, P., and Anstötz, S.: Status of  
1090 IASI instruments onboard Metop-A and Metop-B satellites, 4th IASI International Conference,  
1091 Antibes Juan-Les-Pins, France, 11–15 April 2016, available at:  
1092 [https://iasi.cnes.fr/sites/default/files/drupal/201612/default/bpc\\_iasi-conference4-](https://iasi.cnes.fr/sites/default/files/drupal/201612/default/bpc_iasi-conference4-1_02_instruments_buffet.pdf)  
1093 [1\\_02\\_instruments\\_buffet.pdf](https://iasi.cnes.fr/sites/default/files/drupal/201612/default/bpc_iasi-conference4-1_02_instruments_buffet.pdf) (last access: 30 August 2018), 2016.

1094

1095 Butler, A. H., M. Polvani, and C. Deser: Separating the stratospheric and tropospheric pathways  
1096 of El Niño–Southern Oscillation teleconnections, *Environ. Res. Lett.*, 9, 2, 024014,  
1097 doi:10.1088/1748-9326/9/2/024014, 2014.

1098

1099 Cagnazzo, C., E. Manzini, N. Calvo, A. Douglass, H. Akiyoshi, S. Bekki, M. Chipperfield, M.  
1100 Dameris, M. Deushi, A. M. Fischer, H. Garny, A. Gettelman, M. A. Giorgetta, D. Plummer, E.  
1101 Rozanov, T. G. Shepherd, K. Shibata, A. Stenke, H. Struthers and W. Tian: Northern winter  
1102 stratospheric temperature and ozone responses to ENSO inferred from an ensemble of Chemistry  
1103 Climate Models, *Atmos. Chem. Phys.*, 9, 8935–8948, [www.atmos-chem-phys.net/9/8935/2009/](http://www.atmos-chem-phys.net/9/8935/2009/),  
1104 2009.

1105

1106 Chabrillat, S., Vigouroux, C., Christophe, Y., Engel, A., Errera, Q., Minganti, D., Monge-Sanz,  
1107 B. M., Segers, A., and Mahieu, E.: Comparison of mean age of air in five reanalyses using the  
1108 BASCOE transport model, *Atmos. Chem. Phys.*, 18, 14715–14735, 2018.

1109

1110 Chipperfield, M. P., Kinnersley, J. S., and Zawodny, J.: A twodimensional model study of the  
1111 QBO signal in SAGE II NO<sub>2</sub> and O<sub>3</sub>, *Geophys. Res. Lett.*, 21, 589–592, 1994.

1112

1113 Chubachi, S.: Preliminary results of ozone observations at Syowa Station from February 1982 to  
1114 January 1983, in: *Proc. Sixth Symposium on Polar Meteorology and Glaciology*, edited by:  
1115 Kusunoki, K., vol. 34 of *Mem. National Institute of Polar Research Special Issue*, 13–19, 1984.

1116

1117 Clarisse, L., Clerbaux, C., Franco, B., Hadji-Lazaro, J., Whitburn, S., Kopp, A. K., D. Hurtmans  
1118 and P.-F. Coheur: A decadal data set of global atmospheric dust retrieved from IASI satellite  
1119 measurements, *J. Geophys. Res.*, 124, <https://doi.org/10.1029/2018JD029701>, 2019.

1120

1121 Coldewey-Egbers, M., D. G. Loyola R., P. Braesicke, M. Dameris, M. van Roozendaal, C. Lerot,  
1122 and W. Zimmer: A new health check of the ozone layer at global and regional scales, *Geophys.*  
1123 *Res. Lett.*, 41, 4363–4372, doi:10.1002/2014GL060212, 2014.

1124

1125 Clerbaux, C., A. Boynard, L. Clarisse, M. George, J. Hadji-Lazaro, H. Herbin, D. Hurtmans, M.  
1126 Pommier, A. Razavi, S. Turquety, C. Wespes, and P.-F. Coheur: Monitoring of atmospheric  
1127 composition using the thermal infrared IASI/MetOp sounder, *Atmos. Chem. Phys.*, 9, 6041–  
1128 6054, 2009.

1129

1130 Clerbaux, C. and Crevoisier, C.: New Directions: Infrared remote sensing of the troposphere  
1131 from satellite: Less, but better, *Atmos. Environ.*, 72, 24–26, 2013.

1132

1133 Cochran, D. and Orcutt, G. H.: Application of least squares regression to relationships  
1134 containing auto-correlated error terms, *J. Am. Stat. Assoc.*, 44, 32–61, 1949.

1135

1136 Crevoisier, C., Clerbaux, C., Guidard, V., Phulpin, T., Armante, R., Barret, B., Camy-Peyret, C.,  
1137 Chaboureaud, J.-P., Coheur, P.-F., Crépeau, L., Dufour, G., Labonnote, L., Lavanant, L., Hadji-  
1138 Lazaro, J., Herbin, H., Jacquinet-Husson, N., Payan, S., Péquignot, E., Pierangelo, C., Sellitto,  
1139 P., and Stubenrauch, C.: Towards IASI-New Generation (IASI-NG): impact of improved

1140 spectral resolution and radiometric noise on the retrieval of thermodynamic, chemistry and  
1141 climate variables, *Atmos. Meas. Tech.*, 7, 4367–4385, 2014.

1142

1143 Crutzen, P. J.: Estimates of possible future ozone reductions from continued use of fluoro-  
1144 chloro-methanes (CF<sub>2</sub>Cl<sub>2</sub>, CFC13), *Geophys. Res. Lett.*, 1, 205–208,  
1145 <https://doi.org/10.1029/GL001i005p00205>, 1974.

1146

1147 Dhomse, S., Weber, M., Wohltmann, I., Rex, M., and Burrows, J. P.: On the possible causes of  
1148 recent increases in northern hemispheric total ozone from a statistical analysis of satellite data  
1149 from 1979 to 2003, *Atm. Chem. Phys.*, 6, 1165–1180, 2006.

1150

1151 Dhomse, S. S., Chipperfield, P., Feng, W., Hossaini, R., Mann G. W., and Santee, M. L.:  
1152 Revisiting the hemispheric asymmetry in midlatitude ozone changes following the Mount  
1153 Pinatubo eruption: A 3-D model study, *Geophys. Res. Lett.*, 42, 3038–3047, 2015.

1154

1155 Domeisen, D. I., Garfinkel, C. I., and Butler, A. H.: The teleconnection of El Niño Southern  
1156 Oscillation to the stratosphere, *Reviews of Geophysics*, 57,  
1157 <https://doi.org/10.1029/2018RG000596>, 2019.

1158

1159 Errera, Q., S. Chabrillat, Y. Christophe, J. Debossher, D. Hubert, W. Lahoz, M. Santee, M.  
1160 Shiotani, S. Skachko, T. von Clarmann, and K. Walker: Reanalysis of Aura MLS Chemical  
1161 Observations submitted to *Atms. Chem. Phys. Discuss.*, doi:10.5194/acp-2019-530, 2019.

1162

1163 Farman, J. C., Gardiner, B. G., and Shanklin, J. D.: Large losses of total ozone in Antarctica  
1164 reveal seasonal ClO<sub>x</sub>/NO<sub>x</sub> interaction, *Nature*, 315, 207–210, doi:10.1038/315207a0, 1985.

1165

1166 Farmer, C. B., G. C. Toon, P. W. Shaper, J. F. Blavier, and L. L. Lowes, Stratospheric trace  
1167 gases in the spring 1986 Antarctic atmosphere, *Nature*, 329, 126–130, 1987.

1168

1169 Fioletov, V. E. and Shepherd, T. G.: Seasonal persistence of midlatitude total ozone anomalies,  
1170 *Geophys. Res. Lett.*, 30, 1417, doi:10.1029/2002GL016739, 2003.

1171

1172 Fioletov, V. E. and Shepherd, T. G.: Summertime total ozone variations over middle and polar  
1173 latitudes, *Geophys. Res. Lett.*, 32, 4807, doi:10.1029/2004GL022080, 2005.

1174

1175 Fishman, J., J.K. Creilson, A.E. Wozniak, and P.J. Crutzen, The interannual variability of  
1176 stratospheric and tropospheric ozone determined from satellite measurements, *J. Geophys. Res.*,  
1177 110, D20306, doi:10.1029/2005JD005868, 2005.

1178

1179 Frossard, L., H.E. Rieder, M. Ribatet, J. Staehelin, J. A. Maeder, S. Di Rocco, A. C. Davison, T.  
1180 Pete.: On the relationship between total ozone and atmospheric dynamics and chemistry at mid-  
1181 latitudes – Part 1: Statistical models and spatial fingerprints of atmospheric dynamics and  
1182 chemistry, *Atmos. Chem. Phys.*, 13, 147–164, doi:10.5194/acp-13-147-2013, 2013.

1183

1184 Fusco, A. C. and Salby, M. L.: Interannual variations of total ozone and their relationship to  
1185 variations of planetary wave activity, *J. Clim.*, 12, 1619–1629, 1999.  
1186

1187 Galytzka, E., Rozanov, A., Chipperfield, M. P., Dhomse, Sandip. S., Weber, M., Arosio, C.,  
1188 Feng, W., and Burrows, J. P.: Dynamically controlled ozone decline in the tropical mid-  
1189 stratosphere observed by SCIAMACHY, *Atmos. Chem. Phys.*, 19, 767-783,  
1190 <https://doi.org/10.5194/acp-19-767-2019>, 2019.  
1191

1192 Gebhardt, C., Rozanov, A., Hommel, R., Weber, M., Bovensmann, H., Burrows, J. P.,  
1193 Degenstein, D., Froidevaux, L., and Thompson, A. M.: Stratospheric ozone trends and variability  
1194 as seen by SCIAMACHY from 2002 to 2012, *Atmos. chem. Phys.*, 14, 831–846,  
1195 <https://doi.org/10.5194/acp-14-831-2014>, 2014.  
1196

1197 Harris, N. R. P., Hassler, B., Tummon, F., Bodeker, G. E., Hubert, D., Petropavlovskikh, I.,  
1198 Steinbrecht, W., Anderson, J., Bhartia, P. K., Boone, C. D., Bourassa, A., Davis, S. M.,  
1199 Degenstein, D., Delcloo, A., Frith, S. M., Froidevaux, L., Godin-Beekmann, S., Jones, N.,  
1200 Kurylo, M. J., Kyrölä, E., Laine, M., Leblanc, S. T., Lambert, J.-C., Liley, B., Mahieu, E.,  
1201 Maycock, A., De Mazière, M., Parrish, A., Querel, R., Rosenlof, K. H., Roth, C., Sioris, C.,  
1202 Staehelin, J., Stolarski, R. S., Stübi, R., Tamminen, J., Vigouroux, C., Walker, K. A., Wang, H.  
1203 J., Wild, J., and Zawodny, J. M.: Past changes in the vertical distribution of ozone – Part 3:  
1204 Analysis and interpretation of trends, *Atmos. Chem. Phys.*, 15, 9965-9982,  
1205 <https://doi.org/10.5194/acp-15-9965-2015>, 2015.  
1206

1207 Harrison, D. E., and Larkin, N. K.: El Niño-Southern Oscillation sea surface temperature and  
1208 wind anomalies, 1946–1993, *Rev. Geophys.*, 36, 353–399, doi:10.1029/98RG00715, 1998.  
1209

1210 Hilton, F., R. Armante, T. August, et al. : Hyperspectral Earth Observation from IASI: Five  
1211 Years of Accomplishments, *Bulletin of the American Meteorological Society*, vol. 93, issue 3,  
1212 pp. 347-370, 2012.  
1213

1214 Hofmann, D. J. and Solomon, S.: Ozone destruction through heterogeneous chemistry following  
1215 the eruption of El Chichón, *J. Geophys. Res.*, 94, 5029,  
1216 <https://doi.org/10.1029/JD094iD04p05029>, 1989.  
1217

1218 Hofmann, D. J., S. J. Oltmans, Antarctic ozone during 1992: Evidence for Pinatubo volcanic  
1219 aerosol effects. *J. Geophys. Res.* 98, 18555–18561, doi:10.1029/93JD02092, 1993.  
1220

1221 Hofmann, D. J., S. J. Oltmans, J. M. Harris, B. J. Johnson, and J. A. Lathrop: Ten years of  
1222 ozonesonde measurements at the south pole: Implications for recovery of springtime Antarctic  
1223 ozone, *J. Geophys. Res.*, 102(D7), 8931– 8943, doi:10.1029/96JD03749, 1997.  
1224

1225 Hood, L. L., McCormick, J. P., and Labitzke, K.: An investigation of dynamical contributions to  
1226 midlatitude ozone trends in winter, *J. Geophys. Res.*, 102, 13 079–13 093, 1997.  
1227

1228 Hood, L. L., and B. E. Soukharev: Quasi-decadal variability of the tropical lower stratosphere:  
1229 The role of extratropical wave forcing, *J. Atmos. Sci.*, 60, 2389–2403, 2003.  
1230

1231 Hood, L. L., and B. E. Soukharev: Solar induced variations of odd nitrogen: Multiple regression  
1232 analysis of UARS HALOE data, *Geophys. Res. Lett.*, doi:10.1029/2006GL028122, 2006.  
1233

1234 Hubert, D., Lambert, J.-C., Verhoelst, T., Granville, J., Keppens, A., Baray, J.-L., Bourassa, A.  
1235 E., Cortesi, U., Degenstein, D. A., Froidevaux, L., Godin-Beekmann, S., Hoppel, K. W.,  
1236 Johnson, B. J., Kyrölä, E., Leblanc, T., Lichtenberg, G., Marchand, M., McElroy, C. T.,  
1237 Murtagh, D., Nakane, H., Portafaix, T., Querel, R., Russell III, J. M., Salvador, J., Smit, H. G. J.,  
1238 Stebel, K., Steinbrecht, W., Strawbridge, K. B., Stübi, R., Swart, D. P. J., Taha, G., Tarasick, D.  
1239 W., Thompson, A. M., Urban, J., van Gijsel, J. A. E., Van Malderen, R., von der Gathen, P.,  
1240 Walker, K. A., Wolfram, E., and Zawodny, J. M.: Ground-based assessment of the bias and long-  
1241 term stability of 14 limb and occultation ozone profile data records, *Atmos. Meas. Tech.*, 9,  
1242 2497-2534, <https://doi.org/10.5194/amt-9-2497-2016>, 2016.  
1243

1244 Hurrell, J. W.: Decadal trends in the North Atlantic Oscillation regional temperatures and  
1245 precipitation, *Science*, 269, 676–679, 1995.  
1246

1247 Hurtmans, D., P. Coheur, C. Wespes, L. Clarisse, O. Scharf, C. Clerbaux, J. Hadji-Lazaro, M.  
1248 George, and S. Turquety: FORLI radiative transfer and retrieval code for IASI, *Journal of*  
1249 *Quantitative Spectroscopy and Radiative Transfer*, 113, 1391-1408, 2012.  
1250

1251 Jackman, C., E. Fleming, and F. Vitt: Influence of extremely large solar proton events in a  
1252 changing stratosphere, *J. Geophys. Res.*, 105, 11 659–11 670, 2000.  
1253

1254 Jonsson, A. I., de Grandpré, J., Fomichev, V. I., McConnell, J. C., and Beagley, S. R.: Doubled  
1255 CO<sub>2</sub>-induced cooling in the middle atmosphere: photochemical analysis of the ozone radiative  
1256 feedback, *J. Geophys. Res.*, 109, D24103, <https://doi.org/10.1029/2004JD005093>, 2004.  
1257

1258 Kalnay, E., M. Kanamitsu, R. Kistler, W. Collins, D. Deaven, L. Gandin, M. Iredell, S. Saha, G.  
1259 White, J. Woollen, Y. Zhu, M. Chelliah, W. Ebisuzaki, W. Higgins, J. Janowiak, K.C. Mo, C.  
1260 Ropelewski, J. Wang, A. Leetmaa, R. Reynolds, R. Jenne, and D. Joseph, 1996: The  
1261 NCEP/NCAR 40-Year Reanalysis Project. *Bull. Amer. Meteor. Soc.*, 77, 437–472,  
1262 <https://doi.org/10.1175/1520-0477>, 1996.  
1263

1264 Keeble, J., Brown, H., Abraham, N. L., Harris, N. R. P., and Pyle, J. A.: On ozone trend  
1265 detection: using coupled chemistry–climate simulations to investigate early signs of total column  
1266 ozone recovery, *Atmos. Chem. Phys.*, 18, 7625-7637, <https://doi.org/10.5194/acp-18-7625-2018>,  
1267 2018.  
1268

1269 Keppens, A., J.-C. Lambert, J. Granville, D. Hubert, T. Verhoelst, S. Compernelle, B. Latter, B.  
1270 Kerridge, R. Siddans, A. Boynard, J. Hadji-Lazaro, C. Clerbaux, C. Wespes, D. R. Hurtmans, P.-  
1271 F. Coheur, J. van Peet, R. van der A, K. Garane, M. E. Koukouli, D. S. Balis, A. Delcloo, R.  
1272 Kivi, R. Stübi, S. Godin-Beekmann, M. Van Roozendaal, C. Zehner: Quality assessment of the

1273 Ozone\_cci Climate Research Data Package (release 2017): 2. Ground-based validation of nadir  
1274 ozone profile data products, in preparation for this QOS special issue.  
1275

1276 Kyrölä, E., Laine, M., Sofieva, V., Tamminen, J., Päivärinta, S.-M., Tukiainen, S., Zawodny, J.,  
1277 and Thomason, L.: Combined SAGE II-GOMOS ozone profile data set for 1984–2011 and trend  
1278 analysis of the vertical distribution of ozone, *Atmos. Chem. Phys.*, 13, 10645–10658,  
1279 <https://doi.org/10.5194/acp-13-10645-2013>, 2013.  
1280

1281 Kodera, K. and Kuroda, Y.: Dynamical response to the solar cycle: Winter stratopause and lower  
1282 stratosphere, *J. Geophys. Res.*, 107, 4749, doi:310.1029/2002JD002224, 2002.  
1283

1284 Kuttippurath, J., F. Lefèvre, J.-P. Pommereau, H. K. Roscoe, F. Goutail, A. Pazmiño, J. D.  
1285 Shanklin, Antarctic ozone loss in 1979–2010: First sign of ozone recovery. *Atmos. Chem. Phys.*  
1286 13, 1625–1635, doi:10.5194/acp-13-1625-2013, 2013.  
1287

1288 Kuttippurath, J., and P.J. Nair: The signs of Antarctic ozone hole recovery 2017, *Scientific*  
1289 *Reports*, 7, 585, doi:10.1038/s41598-017-00722-7, 2017.  
1290

1291 Kuttippurath, J., P. Kumar, P.J. Nair, P.C. Pandey: Emergence of ozone recovery evidenced by  
1292 reduction in the occurrence of Antarctic ozone loss saturation, *Climate and Atmospheric Science*,  
1293 1, 42, 2397-3722, doi: 10.1038/s41612-018-0052-6, 2018.  
1294

1295 Labitzke, K. and van Loon, H.: The QBO effect on the solar signal in the global stratosphere in  
1296 the winter of the Northern Hemisphere, *J. Atmos. Solar-Terr. Phys.*, 62, 621–628, 2000.  
1297

1298 Mäder, J. A., J. Staehelin, D. Brunner, W.A. Stahel, I. Wohltmann, and T. Peter: Statistical  
1299 modelling of total ozone: Selection of appropriate explanatory variables, *J. Geophys. Res.*, 112,  
1300 D11108, doi:10.1029/2006JD007694, 2007.  
1301

1302 Mäder, J. A., J. Staehelin, T. Peter, D. Brunner, H. E. Rieder, and W. A. Stahel: Evidence for the  
1303 effectiveness of the Montreal Protocol to protect the ozone layer, *Atmos. Chem. Phys.*, 10, 24,  
1304 12,161–12,171, doi:10.5194/acp-10-12161-2010, 2010.

1305 Manatsa, D. and G. Mukwada: A connection from stratospheric ozone to El Niño-Southern  
1306 Oscillation, *Scientific Reports*, 7, 5558, DOI:10.1038/s41598-017-05111-8, 2017.

1307 Manzini, E., Giorgetta, M. A., Esch, M., Kornblueh, L., and Roeckner, E.: The influence of sea  
1308 surface temperatures on the northern winter stratosphere: Ensemble simulations with the  
1309 MAECHAM5 model, *J. Climate*, 19, 3863–3881, 2006.  
1310

1311 McCormack, J. P., D. E. Siskind, and L. L. Hood: Solar-QBO interaction and its impact on  
1312 stratospheric ozone in a zonally averaged photochemical transport model of the middle  
1313 atmosphere, *J. Geophys. Res.*, 112, D16109, doi:10.1029/2006JD008369, 2007.  
1314

1315 McPeters, R. D., G.J. Labow, and J.A. Logan: Ozone climatological profiles for satellite retrieval  
1316 algorithms, *J. Geophys. Res.-Atmos.*, 112, D05308, doi:10.1029/2005JD006823, 2007.  
1317

1318 Molina, M. J. and Rowland, F. S.: Stratospheric sink for chlorofluoromethanes: Chlorine atom-  
1319 catalysed destruction of ozone, *Nature*, 249, 810–812, 1974.  
1320

1321 Nair, P. J., Froidevaux, L., Kuttippurath, J., Zawodny, J. M., Russell, J. M., Steinbrecht, W.,  
1322 Claude, H., Leblanc, T., van Gijssel, J. A. E., Johnson, B., Swart, D. P. J., Thomas, A., Querel, R.,  
1323 Wang, R., and Anderson, J.: Subtropical and midlatitude ozone trends in the stratosphere:  
1324 Implications for recovery, *J. Geophys. Res.-Atmos.*, 120, 7247–7257,  
1325 <https://doi.org/10.1002/2014JD022371>, 2015.  
1326

1327 Newchurch, M. J., Yang, E.-S., Cunnold, D. M., Reinsel, G. C., Zawodny, J. M., and Russell III,  
1328 J. M.: Evidence for slowdown in stratospheric ozone loss: First stage of ozone recovery, *J.*  
1329 *Geophys. Res.*, 108, 4507, doi:10.1029/2003JD003471, 2003.  
1330

1331 Newman, P. A., Nash, E. R., Kawa, S. R., Montzka, S. A., and Schauffler, S. M.: When will the  
1332 Antarctic ozone hole recover?: *Geophys. Res. Lett.*, 33, L12814, doi:10.1029/2005GL025232,  
1333 2006.  
1334

1335 Oman, L. D., Douglass, A. R., Ziemke, J. R., Rodriguez, J. M., Waugh, D. W., and Nielsen, J.  
1336 E.: The ozone response to ENSO in Aura satellite measurements and a chemistry–climate  
1337 simulation, *J. Geophys. Res.-Atmos.*, 118, 965–976, 2013.  
1338

1339 Pawson, S., Steinbrecht, W., Charlton-Perez, A J Fujiwara, M., Karpechko, A. Y.,  
1340 Petropavlovskikh, I., Urban, J., and Weber, M.: Update on Global Ozone: Past, Present, and  
1341 Future, in: *Scientific Assessment of Ozone Depletion: 2014*, World Meteorological  
1342 Organization, Global Ozone Research and Monitoring Project – Report No. 55, chap. 2, World  
1343 Meteorological Organization/UNEP, 2014.  
1344

1345 Portmann, R. W., S. Solomon, R. R. Garcia, L. W. Thomason, L. R. Poole, M. P. McCormick,  
1346 Role of aerosol variations in anthropogenic ozone depletion in the polar regions. *J. Geophys.*  
1347 *Res.* 101, 22991–23006, doi:10.1029/96JD02608, 1996.  
1348

1349 Knudsen, B. M. and Grooss, J.: Northern midlatitude stratospheric ozone dilution in spring  
1350 modeled with simulated mixing, *J. Geophys. Res.*, 105, 6885–6890, 2000.  
1351

1352 Randel, W. J. and Cobb, J. B.: Coherent variations of monthly mean total ozone and lower  
1353 stratospheric temperature, *J. Geophys. Res.-Atmos.*, 99, 5433–5447, 1994.  
1354

1355 Randel, W. J. and F. Wu: Isolation of the ozone QBO in SAGE II data by singular-value  
1356 decomposition, *J. Atmos. Sci.*, 53, 2546– 2559, 1996.  
1357

1358 Randel, W. J., F. Wu, and R. Stolarski: Changes in column ozone correlated with the  
1359 stratospheric EP flux, *J. Meteorol. Soc. Jpn.*, 80, 849–862, 2002.

1360  
1361 Randel, W. J., Garcia, R. R., Calvo, N., and Marsh, D.: ENSO influence on zonal mean  
1362 temperature and ozone in the tropical lower stratosphere, *Geophys. Res. Lett.*, 36, L15822,  
1363 <https://doi.org/10.1029/2009GL039343>, 2009.  
1364  
1365 Randel, W. J., and A. M. Thompson: Interannual variability and trends in tropical ozone derived  
1366 from SAGE II satellite data and SHADOZ ozonesondes, *J. Geophys. Res.*, 116, D07303,  
1367 doi:10.1029/2010JD015195, 2011.  
1368  
1369 Reinsel, G. C., Miller, A. J., Weatherhead, E. C., Flynn, L. E., Nagatani, R. M., Tiao, G. C., and  
1370 Wuebbles, D. J.: Trend analysis of total ozone data for turnaround and dynamical contributions,  
1371 *J. Geophys. Res.*, 110, D16306, doi:10.1029/2004JD004662, 2005.  
1372  
1373 Revell, L. E., Stenke, A., Luo, B., Kremser, S., Rozanov, E., Sukhodolov, T., and Peter, T.:  
1374 Impacts of Mt Pinatubo volcanic aerosol on the tropical stratosphere in chemistry–climate model  
1375 simulations using CCM1 and CMIP6 stratospheric aerosol data, *Atmos. Chem. Phys.*, 17, 13139–  
1376 13150, 2017.  
1377  
1378 Rex, M., Salawitch, R. J., von der Gathen, P., Harris, N. R. P., Chipperfield, M. P., and  
1379 Naujokat, B.: Arctic ozone loss and climate change, *Geophys. Res. Lett.*, 32, L04116,  
1380 doi:10.1029/2003GL018844, 2004.  
1381  
1382 Rieder, H. E., Frossard, L., Ribatet, M., Staehelin, J., Maeder, J. A., Di Rocco, S., Davison, A.  
1383 C., Peter, T., Weihs, P., and Holawe, F.: On the relationship between total ozone and atmospheric  
1384 dynamics and chemistry at mid-latitudes – Part 2: The effects of the El Niño/Southern  
1385 Oscillation, volcanic eruptions and contributions of atmospheric dynamics and chemistry to  
1386 long-term total ozone changes, *Atmos. Chem. Phys.*, 13, 165–179, 2013.  
1387  
1388 Rind, D., Perlwitz, J., and Lonergan, P.: AO/NAO response to climate change: 1. Respective  
1389 influences of stratospheric and tropospheric climate changes, *J. Geophys. Res.*, 110, D12107,  
1390 doi: 10.1029/2004JD005103, 2005.  
1391  
1392 Rodgers, C. D.: *Inverse Methods for Atmospheric Sounding: Theory and Practice*, World  
1393 Scientific, Series on Atmospheric, Oceanic and Planetary Physics, 2, Hackensack, N. J., 2000.  
1394  
1395 Roscoe, H. K. and Haigh, J. D.: Influences of ozone depletion, the solar cycle and the QBO on  
1396 the Southern Annular Mode, *Q. J. Roy. Met. Soc.*, 133, 1855–1864, 2007.  
1397  
1398 Salby, M., E. Titova, and L. Deschamps: Rebound of Antarctic ozone, *Geophys. Res. Lett.*, 38,  
1399 L09702, doi:10.1029/2011GL047266, 2011.  
1400  
1401 Schnadt, C. and Dameris, M.: Relationship between North Atlantic Oscillation changes and  
1402 stratospheric ozone recovery in the Northern Hemisphere in a chemistry-climate model, *J.*  
1403 *Geophys. Res.*, 30, 1487, doi:10.1029/2003GL017006, 2003.  
1404



1405 Shepherd, T. G., Plummer, D. A., Scinocca, J. F., Hegglin, M. I., Fioletov, V. E., Reader, M. C.,  
1406 Remsberg, E., von Clarmann, T., and Wang, H. J.: Reconciliation of halogen-induced ozone loss  
1407 with the total-column ozone record, *Nat. Geosci.*, 7, 443–449, <https://doi.org/10.1038/ngeo2155>,  
1408 2014.

1409  
1410 Sioris, C. E., McLinden, C. A., Fioletov, V. E., Adams, C., Zawodny, J. M., Bourassa, A. E.,  
1411 Roth, C. Z., and Degenstein, D. A.: Trend and variability in ozone in the tropical lower  
1412 stratosphere over 2.5 solar cycles observed by SAGE II and OSIRIS, *Atmos. Chem. Phys.*, 14,  
1413 3479–3496, <https://doi.org/10.5194/acp-14-3479-2014>, 2014.

1414  
1415 Sofieva, V. F., Kyrölä, E., Laine, M., Tamminen, J., Degenstein, D., Bourassa, A., Roth, C.,  
1416 Zawada, D., Weber, M., Rozanov, A., Rahpoe, N., Stiller, G., Laeng, A., von Clarmann, T.,  
1417 Walker, K. A., Sheese, P., Hubert, D., van Roozendaal, M., Zehner, C., Damadeo, R., Zawodny,  
1418 J., Kramarova, N., and Bhartia, P. K.: Merged SAGE II, Ozone\_cci and OMPS ozone profile  
1419 dataset and evaluation of ozone trends in the stratosphere, *Atmos. Chem. Phys.*, 17, 12533–  
1420 12552, <https://doi.org/10.5194/acp-17-12533-2017>, 2017.

1421  
1422 Solomon, S., R. R. Garcia, F. S. Rowland, and D. J. Wuebbles, On the depletion of Antarctic  
1423 zone, *Nature*, 321, 755–758, 1986.

1424  
1425 Solomon, S., Portman, R. W., Garcia, R. R., Thomason, L. W., Poole, L. R., and McCormack,  
1426 M. P.: The role of aerosol variations in anthropogenic ozone depletion at northern midlatitudes,  
1427 *J. Geophys. Res.*, 101, 6713–6727, 1996.

1428  
1429 Solomon, S.: Stratospheric ozone depletion: A review of concepts and history. *Rev. Geophys.*  
1430 37, 275–316, doi:10.1029/1999RG900008, 1999.

1431  
1432 Solomon, P., Barrett, J., Mooney, T., Connor, B., Parrish, A., and Siskind, D. E.: Rise and  
1433 decline of active chlorine in the stratosphere, *Geophys. Res. Lett.*, 33, L18807,  
1434 <https://doi.org/10.1029/2006GL027029>, 2006.

1435  
1436 Solomon, S., Ivy, D. J., Kinnison, D., Mills, M. J., Neely, R. R., and Schmidt, A.: Emergence of  
1437 healing in the Antarctic ozone layer, *Science*, 353, 269–274,  
1438 <https://doi.org/10.1126/science.aae0061>, 2016.

1439  
1440 Stolarski, R. S., A. J. Krueger, M. R. Schoeberl, R. D. Mc-Peters, P. A. Newman, and J. C.  
1441 Alpert, Nimbus 7 satellite measurements of the springtime Antarctic ozone decrease, *Nature*,  
1442 322, 808–811, 1986.

1443  
1444 Soukharev, B. E. and L. L. Hood: Solar cycle variation of stratospheric ozone: Multiple  
1445 regression analysis of long-term satellite data sets and comparisons with models, *J. Geophys.*  
1446 *Res.*, 111, D20314, doi:10.1029/2006JD007107, 2006.

1447

1448 Steinbrecht, W., H. Claude, U. Köhler, and K. P. Hoinka: Correlations between tropopause  
1449 height and total ozone: Implications for long-term changes, *J. Geophys. Res.*, *103*, 19,183–  
1450 19,192, doi:10.1029/98JD01929, 1998.

1451

1452 Steinbrecht, W., B. Hassler, H. Claude, P. Winkler, and R. S. Stolarski: Global distribution of  
1453 total ozone and lower stratospheric temperature variations, *Atmos. Chem. Phys.*, *3*, 1421–1438,  
1454 2003.

1455

1456 Steinbrecht, W., et al.: Interannual variation patterns of total ozone and lower stratospheric  
1457 temperature in observations and model simulations, *Atmos. Chem. Phys.*, *6*, 349–374,  
1458 doi:10.5194/acp-6-349-2006, 2006

1459

1460 Steinbrecht, W., Froidevaux, L., Fuller, R., Wang, R., Anderson, J., Roth, C., Bourassa, A.,  
1461 Degenstein, D., Damadeo, R., Zawodny, J., Frith, S., McPeters, R., Bhartia, P., Wild, J., Long,  
1462 C., Davis, S., Rosenlof, K., Sofieva, V., Walker, K., Ralpoe, N., Rozanov, A., Weber, M.,  
1463 Laeng, A., von Clarmann, T., Stiller, G., Kramarova, N., Godin-Beekmann, S., Leblanc, T.,  
1464 Querel, R., Swart, D., Boyd, I., Hocke, K., Kämpfer, N., Maillard Barras, E., Moreira, L.,  
1465 Nedoluha, G., Vigouroux, C., Blumenstock, T., Schneider, M., García, O., Jones, N., Mahieu, E.,  
1466 Smale, D., Kotkamp, M., Robinson, J., Petropavlovskikh, I., Harris, N., Hassler, B., Hubert, D.,  
1467 and Tummon, F.: An update on ozone profile trends for the period 2000 to 2016, *Atmos. Chem.*  
1468 *Phys.*, *17*, 10675–10690, doi:10.5194/acp-17-10675-2017, 2017.

1469

1470 Thomason, L. W., Ernest, N., Millán, L., Rieger, L., Bourassa, A., Vernier, J.-P., Manney, G.,  
1471 Luo, B., Arfeuille, F., and Peter, T.: A global space-based stratospheric aerosol climatology:  
1472 1979–2016, *Earth Syst. Sci. Data*, *10*, 469-492, <https://doi.org/10.5194/essd-10-469-2018>, 2018.

1473

1474 Thompson, D. W. J. and J.M. Wallace: Annular modes in the extratropical circulation. Part I:  
1475 month-to-month variability, *J. Climate*, *13*, 1000–1016, 2000.

1476

1477 Thompson, D. W. J. and Solomon, S.: Interpretation of Recent Southern Hemisphere Climate  
1478 Change, *Science*, *296*, 895-899, 2002.

1479

1480 Tian, W., M.P. Chipperfield, L.J. Gray, and J.M. Zawodny: Quasi-biennial oscillation and tracer  
1481 distributions in a coupled chemistry-climate model, *J. Geophys. Res.*, *111*, D20301,  
1482 doi:10.1029/2005JD006871, 2006.

1483

1484 Tiao, G. C., G. C. Reinsel, D. Xu, J. H. Pedrick, X. Zhu, A. J. Miller, J. J. DeLuisi, C. L. Mateer,  
1485 and D. J. Wuebbles, Effects of autocorrelation and temporal sampling schemes on estimates of  
1486 trend and spatial correlation, *J. Geophys Res.*, *95*, 20,507-20,517, 1990.

1487

1488 Tweedy, O. V., Waugh, D. W., Randel, W. J., Abalos, M., Oman, L. D. and Kinnison, D. E.: The  
1489 impact of boreal summer ENSO events on tropical lower stratospheric ozone, *J. Geophys. Res.*,  
1490 *Atmospheres*, *123*, 9843–9857, doi:10.1029/2018JD029020, 2018.

1491

1492 Valks, P., N. Hao, S. Gimeno Garcia, D. Loyola, M. Dameris, P. Jöckel, and A. Delcloo:  
1493 Tropical tropospheric ozone column retrieval for GOME-2, *Atmos. Meas. Tech.*, 7, 2513–2530,  
1494 doi:10.5194/amt-7-2513-2014, 2014.  
1495  
1496 Vigouroux, C., Blumenstock, T., Coffey, M., Errera, Q., García, O., Jones, N. B., Hannigan, J.  
1497 W., Hase, F., Liley, B., Mahieu, E., Mellqvist, J., Notholt, J., Palm, M., Persson, G., Schneider,  
1498 M., Servais, C., Smale, D., Thölix, L., and De Mazière, M.: Trends of ozone total columns and  
1499 vertical distribution from FTIR observations at eight NDACC stations around the globe, *Atmos.*  
1500 *Chem. Phys.*, 15, 2915–2933, <https://doi.org/10.5194/acp-15-2915-2015>, 2015.  
1501  
1502 Weatherhead, E.C., G. C. Reinsel, G. C. Tiao, X.-L. Meng, D. Choi, W.-K. Cheang, T. Keller, J.  
1503 DeLuisi, D. J. Wuebbles, J. B. Kerr, A. J. Miller, S. J. Oltmans and J. E. Frederick: Factors  
1504 affecting the detection of trends: Statistical considerations and applications to environmental  
1505 data, *J. Geophys. Res. Atmos.*, 103, 17149–17161, 1998.  
1506  
1507 Weber, M., Dikty, S., Burrows, J. P., Garny, H., Dameris, M., Kubin, A., Abalichin, J., and  
1508 Langematz, U.: The Brewer-Dobson circulation and total ozone from seasonal to decadal time  
1509 scales, *Atmos. Chem. Phys.*, 11, 11221-11235, <https://doi.org/10.5194/acp-11-11221-2011>,  
1510 2011.  
1511  
1512 Weber, M., Coldewey-Egbers, M., Fioletov, V. E., Frith, S. M., Wild, J. D., Burrows, J. P.,  
1513 Long, C. S., and Loyola, D.: Total ozone trends from 1979 to 2016 derived from five merged  
1514 observational datasets – the emergence into ozone recovery, *Atmos. Chem. Phys.*, 18, 2097–  
1515 2117, <https://doi.org/10.5194/acp-18-2097-2018>, 2018.  
1516  
1517 Wespes, C., D. Hurtmans, L.K. Emmons, S. Safieddine, C. Clerbaux, D.P. Edwards, and P.-F.  
1518 Coheur: Ozone variability in the troposphere and the stratosphere from the first six years of IASI  
1519 observations (2008-2013), *Atmos. Chem. Phys.*, 16, 5721-5743, 2016.  
1520  
1521 Wespes, C., D. Hurtmans, C. Clerbaux, and P.-F. Coheur: O<sub>3</sub> variability in the troposphere as  
1522 observed by IASI over 2008–2016 — Contribution of atmospheric chemistry and dynamics, *J.*  
1523 *Geophys. Res. Atmos.*, 122, 2429–2451, doi:10.1002/2016JD025875, 2017.  
1524  
1525 Wespes, C., Hurtmans, D., Clerbaux, C., Boynard, A., and Coheur, P.-F.: Decrease in  
1526 tropospheric O<sub>3</sub> levels in the Northern Hemisphere observed by IASI, *Atmos. Chem. Phys.*, 18,  
1527 6867–6885, <https://doi.org/10.5194/acp-18-6867-2018>, 2018.  
1528  
1529 Witte, J. C., M.R. Schoeberl, A.R. Douglass, and A.M. Thompson: The Quasi-biennial  
1530 Oscillation and annual variations in tropical ozone from SHADOZ and HALOE, *Atmos. Chem.*  
1531 *Phys.*, 8, 3929–3936, 2008.  
1532  
1533 World Meteorological Organization (WMO): Scientific Assessment of Ozone Depletion: 2006,  
1534 Global Ozone Research and Monitoring Project, Report No. 50, Geneva, Switzerland, 2007.  
1535

1536 World Meteorological Organization (WMO): Scientific Assessment of Ozone Depletion: 2010,  
1537 Global Ozone Research and Monitoring Project, Report No. 52, Geneva, Switzerland, 2011.  
1538  
1539 World Meteorological Organization (WMO): Scientific Assessment of Ozone Depletion: 2014,  
1540 Global Ozone Research and Monitoring Project, Report No. 55, Geneva, Switzerland, 2014.  
1541  
1542 World Meteorological Organization (WMO): Scientific Assessment of Ozone Depletion: 2018,  
1543 Global Ozone Research and Monitoring Project, Report No. 58, Geneva, Switzerland, 2018.  
1544  
1545 Wohltmann, I., R. Lehmann, M. Rex, D. Brunner, and J. A. Maeder: A process-oriented  
1546 regression model for column ozone, *J. Geophys. Res.*, *112*, D12304, doi:10.1029/2006JD007573,  
1547 2007.  
1548  
1549 Yang, E.-S., D. M. Cunnold, M. J. Newchurch, R. J. Salawitch, M. P. McCormick, J. M. Russell  
1550 III, J. M. Zawodny, S. J. Oltmans: First stage of Antarctic ozone recovery. *J. Geophys. Res.* *113*,  
1551 D20308, doi:10.1029/2007JD009675, 2008.  
1552  
1553 Zerefos, C. S., Tourpali, K., Bojkov, R., Balis, D., Rognerund, B., and Isaksen, I.: Solar activity  
1554 – total ozone relationships: observations and model studies with heterogeneous chemistry, *J.*  
1555 *Geophys. Res.*, *102*, 1561–1569, 1997.  
1556  
1557 Ziemke, J. R., A.R. Douglass, L.D. Oman, S.E. Strahan, and B.N. Duncan: Tropospheric ozone  
1558 variability in the tropics from ENSO to MJO and shorter timescales, *Atmos. Chem. Phys.*, *15*,  
1559 8037–8049, 2015.